Please cite the Published Version

Additional Information: This is an open access article published in Journal of Geophysical Research: Earth Surface by Wiley.

Data Access Statement: Figure and Table included as Supplementary material in article

Quantifying Bed Surface Roughness in Bedrock and Boulder-Bed Rivers

R. C. Houseago[1,2] , R. A. Hodge[1] , B. Asher[1], R. I. Ferguson[1] , C. R. Hackney[3], R. J. Hardy[1] , T. B. Hoey[4] , J. P. L. Johnson[5] , S. P. Rice[6] , E. M. Yager[7] , and T. Yamasaki[1]

[1]Department of Geography, Durham University, Durham, UK, [2]Geography and Environment, Loughborough University, Loughborough, UK, [3]School of Geography, Politics and Sociology, Newcastle University, Newcastle, UK, [4]Department of Civil and Environmental Engineering, Brunel University London, Uxbridge, UK, [5]Department of Geological Sciences, University of Texas at Austin, Austin, TX, USA, [6]Department of Natural Sciences, Manchester Metropolitan University, Manchester, UK, [7]Center for Ecohydraulics Research, Department of Civil and Environmental Engineering, University of Idaho, Moscow, ID, USA

Abstract The surface roughness of river beds affects flow resistance and sediment transport. In rough-bed rivers (RBRs), where flow is shallow relative to roughness height, the surface roughness is difficult to define due to complex multi-scale roughness elements (bedrock, boulders, and sediment patches). Here, neither the sediment grain size distribution percentiles (e.g., D_{84}) nor the bed elevation standard deviation (Z_σ) fully captures the surface roughness. This paper uses high-resolution digital elevation models of 20 RBR reaches to evaluate their channel morphology and surface roughness. A set of 29 different multi-scale elevation, gradient-based, and area-based, roughness metrics are assessed. Correlation analysis and robust feature selection identified interchangeable metrics, revealing which roughness metrics provided independent information on channel characteristics. Principal component analysis and hierarchical clustering analysis showed that a comprehensive description of RBR topography requires the concurrent use of multiple metrics encompassing (a) a vertical or horizontal scale-based roughness metric, (b) a slope- or area-based metric, and (c) surface elevation skewness or kurtosis. Slope- and area-based metrics can include roughness directionality relative to the bulk flow. We demonstrate how surface roughness metrics, specifically the use of multiple metrics in unison, are suitably capable of representing and distinguishing between RBRs with differing characteristics. In some cases, rivers with different morphology types (e.g., boulder bed or bedrock) are found to have greater similarity in their surface roughness metrics than rivers classified as morphologically similar. We then discuss RBR morphological and roughness characteristics in the context of flow resistance and sediment transport processes.

Plain Language Summary River beds can be made of solid rock (bedrock) with differing amounts of sediment on the bed (from none to fully covered), including boulders (sediment grains larger than 0.265 m wide). We explore how these differing features affect how uneven the shape of the bed surface is; we call this variation in the bed the "surface roughness". It is important to accurately measure how "smooth" or "rough" a river beds is, as this controls how fast water flows and how deep the flow is during flood events. We calculate the surface roughness for 20 river beds using 29 different surface roughness measurements. We show that in order to distinguish between these river beds using their measured surface roughness, we need to use a combination of multiple different measurement types based on: (a) the vertical or horizontal size of the river, (b) the local slope or area of the bed surface, and (c) how much difference there is in height between different areas of the bed (skewness or kurtosis). In the future, this advanced ability to describe the river bed surface roughness will help us to improve our ability to manage rivers, for example, by predicting how deep the river flow will be during floods.

1. Introduction

Rough-bed rivers (RBRs) feature shallow flow depths (d) relative to the bed element height (k), typically in the order of $d/k < 5$, thus the bed surface characteristics strongly influence flow dynamics. To date, there remains a knowledge gap in evaluating the diversity of rough-bed river (RBR) morphology and surface roughness, and the best methods to quantify these characteristics. Quantifying channel geometry and surface roughness is a precursor to understanding their effects on hydraulics and ultimately predicting flow resistance (hydraulic roughness)

Writing – original draft: R. C. Houseago, R. A. Hodge
Writing – review & editing: R. I. Ferguson, C. R. Hackney, R. J. Hardy, T. B. Hoey, J. P. L. Johnson, S. P. Rice, E. M. Yager, T. Yamasaki

(Ferguson, 2022; Powell, 2014). This knowledge further informs flood depths, sediment entrainment and morphological change, including bedrock incision (Inoue et al., 2014; Johnson, 2014). However, there is no consensus on which metrics best represent the influence of channel topography on flow and sediment transport processes in RBRs. Furthermore, the surface roughness and relevant metrics must be evaluated according to the form and processes being studied (Smith, 2014). Herein, "roughness" refers to surface roughness (spatial variability of the surface topography), not hydraulic roughness (resistance to flow due to the channel bed surface) unless explicitly stated. Surface roughness and hydraulic roughness are nonetheless related since surface topography influences velocity distributions in the overlying flow. In rivers, this is the surface roughness magnitude relative to the flow depth. Deeper flows over a river bed will result in lower flow resistance than shallower flows over the same bed, and the near-bed stresses will differ.

The surface roughness of relatively smoother alluvial channels, primarily composed of sand and gravel, has been widely investigated (Aberle & Nikora, 2006; Bertin et al., 2017; Coleman et al., 2011; Simons & Richardson, 1961). In gravel-bed rivers, the flow is typically shallow, with the ratio of flow depth to typical roughness height being 10 to 20 during floods, and below 5 in base flow (Hardy et al., 2009). Flow resistance predictions typically use sediment grain size distribution percentiles (50th, D_{50}; or 84th, D_{84}) or the standard deviation of surface elevations (Z_σ) (Ferguson, 2007; X. Chen et al., 2020). While Z_σ is positively correlated with D_{84}, comparisons between published data reveal differing trends with no universal relationship (X. Chen et al., 2020). These results have been interpreted as indicating that channel properties other than grain size alone contribute to topographic roughness (Pearson et al., 2017; Vázquez-Tarrío et al., 2017).

In RBRs, which cover a continuum spanning from fully bedrock to boulder-bed rivers, the presence of multiple different roughness elements (including variable sediment cover, exposed bedrock, boulders, bed and sidewall roughness) means that D_{84} poorly represents channel roughness. Instead, Z_σ has been proposed as a roughness metric (Barabási & Stanley, 1995) that provides a more representative indication of surface roughness (Aberle & Nikora, 2006; Finnegan et al., 2007; Hodge & Hoey, 2016a; Johnson & Whipple, 2007). In gravel-bed rivers, some authors have found that implementing Z_σ instead of D_{84} improves their accuracy in flow resistance predictions (Aberle & Smart, 2003; Heritage & Milan, 2009; X. Chen et al., 2020). However, at low submergence, as in most rough-bed channels, there remains a substantial uncertainty in predictive accuracy in flow resistance. The uncertainty is potentially due to differing channel morphological groups (e.g., plane bed, step-pool sequences) (X. Chen et al., 2020). From a hydrodynamic perspective, the uncertainty at low submergence may also be attributed to the complex near-bed flow field occupying a substantial portion of the flow depth rather than a small portion when submergence is high. For example, when boulders are present, the flow field becomes complex with plunging flow over obstacles and coherent flow structures formed by the obstacles (Liu et al., 2017; Monsalve et al., 2017).

Roughness in river channels is often directional. For example, the elevation and orientation of bedrock ridges can further modulate flow resistance, with greater resistance occurring when ridges are perpendicular to the flow (Goode & Wohl, 2010a). The spacing of roughness elements, such as boulders, also affects flow resistance, and including boulder concentration metrics into predictive formulas improves velocity predictions (Nitsche et al., 2012; Wiener & Pasternack, 2022; Yager et al., 2007). In rivers with exposed bedrock, flow resistance predictions have assumed that roughness lengths from separate bedrock and sediment patches could be spatially averaged (Ferguson et al., 2019; Inoue et al., 2014; Johnson, 2014). Wiener and Pasternack (2022) noted the limited published data on boulder concentrations in RBRs, highlighting the need to synthesize RBR morphology and surface roughness.

The complexity and variation in length scales present in RBRs make it challenging to define a single representative surface roughness length. New alternative approaches are required to improve calculations of sediment transport and flow resistance in these systems (Ferguson et al., 2019). This first requires identifying additional surface roughness metrics that effectively represent the diversity of RBRs across a range of scales, potentially mitigating the need for separate sediment grain size or boulder spacing metrics. Recent advances in high-resolution survey technology provide a new opportunity to quantify surface roughness and explore the morphometrics of complex RBRs (Gomez-Heras et al., 2019). Channel bed topography and roughness can be quantified using Digital Elevation Model (DEM) data sets obtained from methods such as terrestrial or airborne laser scanning and photogrammetry (Brasington et al., 2012; Heritage & Milan, 2009; Hodge et al., 2009), which capture scale-dependent roughness and remove the reliance on empirical roughness factors (Lane, 2005).

Table 1
Field Data Sites, Geometric Characteristics, and Data Source

Site	w (m)	d (m)	D_{84} (m)	d/D_{84} (−)	S (m/m)	F_e (−)	ρ_b (m²/m²)	Lithology
BirkBeck	12.29	0.74	0.039	19.12	0.013	0.76	0	Sandstone
Garry[a]	15.02	0.47	0.065	7.26	0.011	0.48	0	Schist
Greta1	13.20	0.61	0.039	15.64	0.036	0.98	0	Limestone
Greta3	7.14	0.53	0.116	4.51	0.009	0.10	0	Limestone
Greta4	12.84	0.65	0.047	13.96	0.006	0.98	0	Limestone
HenryMtns	8.73	0.77	0.012	62.96	0.024	0.54	0	Sandstone
Lushui1[b]	62.05	8.18	2.730[d]	2.99	0.030	0.05	0.05	Quartzite/schist
Lushui2[b]	58.29	9.90	2.588[d]	3.82	0.020	0.02	0.11	Quartzite/schist
Lushui3[b]	87.05	10.82	4.383[d]	2.47	0.030	0.07	0.13	Quartzite/schist
Lushui4[b]	67.88	9.73	3.143[d]	3.10	0.030	0.03	0.18	Quartzite/schist
Riedbach3[c]	9.59	0.68	0.230	2.96	0.068	0.00	0.10	Crystalline rocks
Riedbach5[c]	13.62	1.08	0.480	2.24	0.136	0.00	0.142	Crystalline rocks
Riedbach6[c]	11.57	0.85	0.930	0.92	0.337	0.00	0.4	Crystalline rocks
Riedbach7[c]	21.68	2.44	1.180	2.07	0.464	0.00	0.52	Crystalline rocks
Swale	26.11	0.51	0.097	5.22	0.033	0.88	0	Limestone
Tees	33.88	0.71	0.040	17.51	0.033	1.00	0	Dolerite
TroutBeck	10.02	0.52	0.140	3.69	0.020	0.78	0	Limestone
Wharfe1	18.79	0.63	0.056	11.10	0.036	0.90	0	Limestone
Wharfe2	16.71	0.72	0.047	15.26	0.008	0.94	0	Limestone
Wharfe3	15.03	0.99	0.102	9.76	0.001	0.64	0	Limestone

Note. Nomenclature Are Defined in Table 2. Colored Symbols Correspond to Markers Used in Subsequent Data Plots. Data sources: [a] Williams et al. (2022), [b] Carr et al. (2023) and Carr and DiBiase (2024), and [c] Schneider et al. (2015). [d]based on boulders >1 m diameter.

Potential metrics of interest include variance in surface elevation, local gradients, and directional properties of the bed at multiple scales (see details in §2). Multiple metrics are likely to be required, as differing topographies can have the same value for one metric, yet contrasting effects on flow resistance (Ferguson et al., 2024). For example, Chung et al. (2021) evaluated engineered surfaces and proposed that the impact of surface topography on form drag requires evaluation of (a) *roughness height*, an elevation deviation-based metric; (b) *frontal solidity*, a measure of projected frontal area to plan area, or *effective slope*, and (c) *plan solidity*, *skewness* or *solid volume fraction* (defined in §2.3). They suggest that directionality and clustering should also be considered.

This paper aims to quantify the morphology and surface roughness of a comprehensive data set of 20 high-resolution digital elevation models (DEMs) of RBRs of varying scales and characteristics, including boulders and exposed bedrock. We assess 29 surface roughness metrics grouped into three categories: elevation, hybrid elevation-spacing, and multi-scale metrics (defined in §2.3). Multi-scale analysis reveals the minimum set of roughness metrics required to characterize the rough beds. Channel characteristics and morphology's are evaluate in relation to the relative magnitude of certain surface roughness metrics. The results suggest directions for future surface roughness assessments and for quantifying the contribution of channel characteristics to flow resistance.

2. Methods

2.1. Data Acquisition and Pre-Processing

This paper evaluates 20 different river bed surfaces from 10 rivers with varying lithology (Table 1), encompassing a range of channel topographies. Each river bed surface is herein referred to as a "site." High-resolution point clouds were obtained for each site via Structure from Motion (SfM) photogrammetry (sites HenryMtns and Lushui) or Terrestrial Laser Scanner (TLS) (all other sites). Examples of the sites and the corresponding DEMs are shown in Figure 1, and all sites are shown in Supporting Information S1 along with details of the geographical
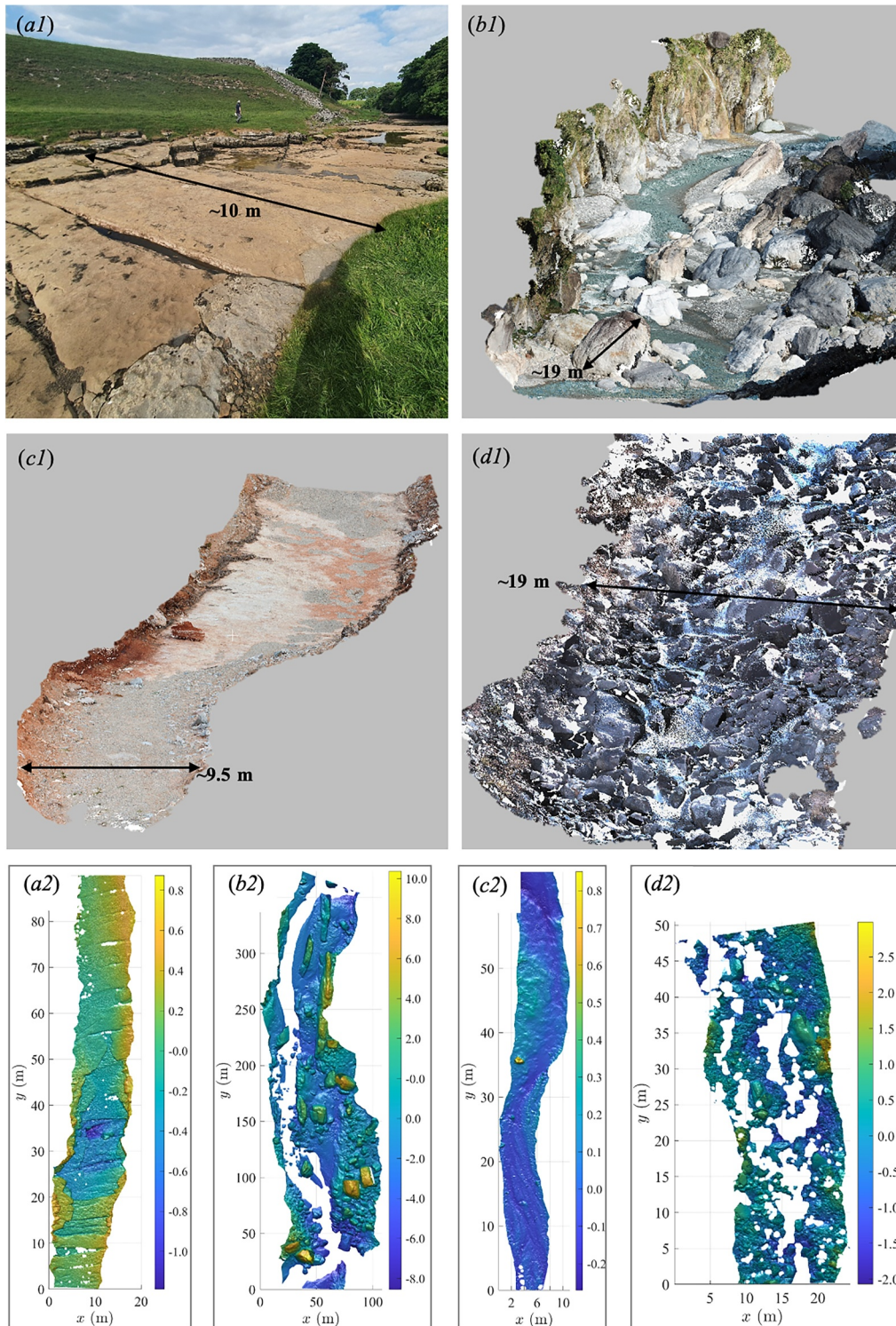
Figure 1. Images of site reaches for sites (a1) Greta1, (b1) Lushui3, (c1) HenryMtns, and (d1) Riedbach7. Channel walls shown in images (a1) to (d1) are excluded from bed surface roughness calculations. Corresponding digital elevation models used for surface roughness calculations are presented in the lower panel (a2 to d2), banks and water (white patches) have been removed. The color bars indicate z elevations (m) of the detrended beds. Flow direction is from bottom to top.

locations. Data from external sources are: Garry (Williams et al., 2022), Lushui (Carr & DiBiase, 2024), and Riedbach (Schneider et al., 2015).

Our focus is on the reach scale, hence each site length is at least several times the bankfull channel width and has consistent morphology. X. Chen et al. (2020) report that a reach length of five times the channel width is sufficient for calculating the standard deviation of elevations. We focus on straight-walled single-thread channels with linear bed gradients along the entire reach. The sites do not include repeating roughness features such as step-pools or alternate bars, hence the lengths are sufficient to appropriately capture the bed roughness features.

Data points outside the channel bankfull elevation, identified based on vegetation lines or a distinct break in the bank topographic slope, were removed to retain only the bank and channel point cloud. In several cases, topographic data was absent from the wetted areas, although this was minimized by data acquisition during very low flows. These gaps were not filled and are shown in Supporting Information S1 figures. Each point cloud was cleaned to remove erroneous data and vegetation, then re-gridded at a horizontal resolution (Δxy) of 0.05 m. It is noted that surface roughness metric magnitude can vary if the point cloud is gridded to a different resolution (Grohmann et al., 2010), hence they are held constant for all sites. After the calculation of bankfull width and depth, the channel banks were identified and removed based on distinct breaks in slope, so roughness metrics were calculated solely from the channel bed. Before calculating surface roughness data, the surfaces were detrended to remove the reach-scale slope (streamwise and transverse) by fitting and subtracting a linear planar surface. Channel reach-scale slope measurements were made before detrending.

2.2. Channel Characteristics: Geometry and Slope

For each site, we present two sets of properties: channel characteristics and surface roughness metrics calculated from the topographic data, as listed in Table 2. The latter include multidimensional metrics (1-, 2- and 3-D).

Channel characteristics include the channel geometry (width, depth, and reach-scale slope), lithology, sediment grain size (84th percentile, D_{84}), and the fraction of exposed bedrock (F_e) relative to the total channel area. F_e was quantified by calculating the spatial coverage from images. Grain size percentiles (D_{84}) for sites we measured were measured by manual image analysis of multiple sediment patches within the channels. Images were scaled using an object of known size, and the size of at least 50 grains was measured in each. D_{84} was averaged between all images from the same site. Boulder density (ρ_b) presents the estimated boulder top-down surface area relative to reach area (full details are provided in source publications), with boulder sizes defined as >1.0 m in Lushui (Carr et al., 2023) and >0.5 m Riedbach (Schneider et al., 2015). Channel reach-scale bed slope (S) was obtained from a linear fit to a long profile extracted along the channel center. Perpendicular cross sections at intervals of 0.5 m were extracted along the channel center line to calculate bankfull channel width, depths, and hydraulic radius (R). Each channel's cross-section width was calculated as the distance between the outermost points, which were averaged to provide the mean bankfull width (w) for the entire reach. The bankfull flow depth (d) was calculated for each cross-sectional and averaged along the entire reach.

2.3. Quantifying Surface Roughness

The topographic properties of each surface were quantified based on a range of roughness metrics (Table 2) spanning elevation, spatial, hybrid, and multi-scale metrics (Hobson, 1972; Smith, 2014). Surface roughness can be calculated over (i) the entire spatial domain of the data set, termed "global" values; or (ii) at multiple scales by sub-sampling using windowing or filtering methods (see §2.3.3), termed "multi-scale" value. There is an abundance of roughness metrics within the literature, yet there is a lack of consensus on the most applicable methods for RBRs. The morphometrics we applied to evaluate surface roughness are detailed herein and summarized in Table 2. The majority of the metrics have been linked to predicting drag (Chung et al., 2021), and thus offer potential for improved flow resistance predictions as discussed in §4.2.

2.3.1. Elevation Metrics

Elevation metrics quantify the vertical elevation properties of a surface, based on the first four moments of the distribution of elevations. The elevation mean deviation (Z_μ) is defined as the mean of the absolute distances between the elevation values and a mean plane fitted to the data. Probability density functions (PDFs) of the

Table 2
Channel Geometry and Surface Roughness Metrics

Metric type	Nomenclature	Metric	Unit
Channel geometry	F_e	Fraction of exposed bedrock	-
	D_{84}	Sediment size (84th percentile)	m
	ρ_b	Boulder density	m^2/m^2
	w	Channel width	m
	d	Channel depth	m
	R	Hydraulic radius	m
	S	Channel reach-scale slope	m/m
Elevation	Z_μ	Elevation mean deviation	m
	Z_R	Elevation range	m
	Z_σ	Elevation standard deviation	m
	Z_{sk}	Elevation skewness	-
	Z_{ku}	Elevation kurtosis	-
Hybrid	Ru_μ	Rugosity, mean	-
	Ru_σ	Rugosity, std. dev.	-
	$S_{l,\mu}$	Local slope, mean	m/m
	$S_{l,\sigma}$	Local slope, std. dev.	m/m
	κ_μ	Surface curvature, mean	m^{-1}
	κ_σ	Surface curvature, std. dev.	m^{-1}
(directional)	I_i	Inclination index	-
(directional)	λ_f	Frontal solidity	-
(directional)	ES	Effective slope	-
(directional)	α_R	Frontal aspect ratio	-
Multi-scale	MB[−]	Metric-Break	defined by base metric
	WB[−]	Window-Break	m
	H^{−}	Hurst exponent	-

Note. Metrics that include a directional component relative to incoming flow are indicated.

elevation data provide several global scale statistics: elevation range ($Z_R = z_{95} - z_5$, where z_{95} and z_5 are the 95th and 5th percentiles, respectively), standard deviation (Z_σ), skewness (Z_{sk}), and kurtosis (Z_{ku}).

2.3.2. Hybrid Metrics

Hybrid metrics are based on both vertical (elevation) and horizontal spacing data. Local slope angles were calculated across the entire surface (gridded at 0.05 m resolution) based on the gradient of greatest descent to 8-neighboring points (Brasington et al., 2012; Grohmann et al., 2010; Schwanghart & Scherler, 2014). From this, we calculate the mean local slope (S_l) and local slope standard deviation ($S_{l,\sigma}$) over the entire DEM. Surface curvature (κ) is the second derivative of the surface elevation, which represents the spatial rate of change of slope, whereby positive values indicate concave surfaces and negative values indicate a convex surface (Grohmann et al., 2010; Olaya, 2009). The surface curvature (profile curvature) is calculated based on a point and its eight immediate neighbors (Olaya, 2009; Schwanghart & Scherler, 2014), from which we calculate the curvature mean (κ_μ), and standard deviation (κ_σ) over the DEM (Grohmann et al., 2010). Profile curvature was chosen over other types (e.g., planform or tangential) to assess downslope curvature and identify breaks in slopes. Rugosity (Ru), also referred to as "Area ratio" in some literature, represents the ratio between the 3-D surface area and corresponding 2-D planform area, whereby unity represents a smooth surface and the value increases for rougher surfaces. It was calculated based on cell area, using a method of triangulation about the central point and 8 neighboring cells (Jenness, 2004). From these values, we calculate the mean (Ru_μ) and standard deviation (Ru_σ)
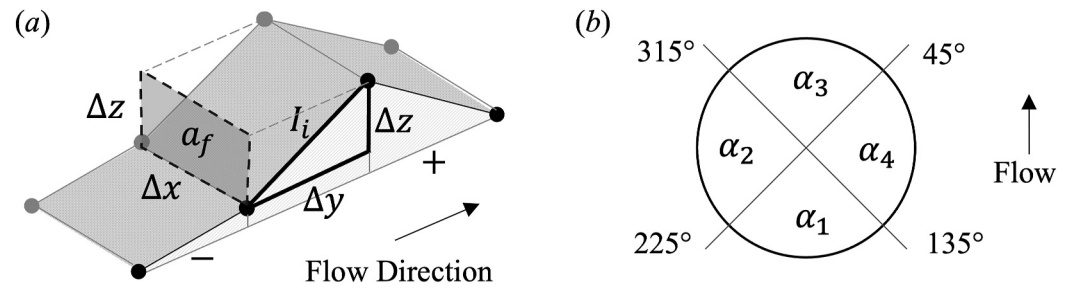
Figure 2. Depiction of components used to calculate the hybrid directional metrics (a) inclination index (I_i) and frontal projected area (a_f) components, and (b) Surface cell aspect ratio quadrants.

over the DEM. These metrics have been selected for calculation based on their ability to quantify topographic variations.

The preceding metrics do not take into account the direction of the surface topography with respect to the bulk downstream flow direction, but topographic orientation has been demonstrated to affect flow resistance (Goode & Wohl, 2010b). We include the following metrics with directional considerations. The inclination index (I_i) is the ratio of upstream to downstream facing cells across the entire point cloud (Hodge et al., 2009; Smart et al., 2004). Whether a cell faces upstream or downstream depends on the elevation of the next downstream cell (e.g., a positive or negative Δz value), as presented in Figure 2a. A negative I_i value indicates a greater proportion of upstream facing slopes, and the point increment spacing is defined by the surface resolution (Δy). The effective slope (Napoli et al., 2008) is defined as the mean absolute cell slope across the gridded DEM, $ES = \langle|\Delta_z/\Delta_y|\rangle$. ES and S_l are similar metrics, while ES provides an absolute value irrespective of flow direction, and is more widely used in engineering practice.

The area exposed to incoming bulk flow is represented by the frontal solidity, $\lambda_f = A_f/A_t$, whereby A_f is the sum of the frontal projected area of all upstream facing cells (a_f) (Figure 2a), and A_t is the total plan area of the entire surface (Chung et al., 2021). It is noted that λ_f does not account for element-element interactions or shadowing effects but provides a first-order indication of directional flow blockage.

Finally, the aspect of each cell was calculated and categorized into one of four quadrants depending on its aspect angle relative to the downstream flow direction, as defined in Figure 2b. The quadrants and respective aspect angles relative to incoming flow (located at 180°) are: α_1 (135–225°), α_2 (225–315°), α_3 (315–45°), α_4 (45–135°). The number of cells in each quadrant is normalized by the total number of cells, such that the sum of all quadrants is unity. Subsequently, a bulk evaluation of the dominant surface directionality is given by $\alpha_R = (\alpha_1 + \alpha_3)/(\alpha_2 + \alpha_4)$; when $\alpha_R > 1$, the surface faces are dominantly perpendicular to the direction of flow.

2.3.3. Multi-Scale Analysis

The final set of methods assesses the calculation of roughness metrics at different spatial scales using a fractal-based approach that eliminates the need to define an arbitrary sampling length.

Multi-scale analysis is applied to elevation and hybrid metrics by calculating them at sampling lengths smaller than the entire surface (i.e., moving windows), which are iteratively increased in size. Window sizes (n) range from 3×3 neighboring cells up to the channel width ($w \cdot \Delta xy$ cells) in 200 logarithmic spaced steps. We then plot the average metric value (averaged across all windows, for a given window size) against the window size to create space-metric log-log plots, comparable to variograms or deviograms for deviation statistics (McCarroll & Nesje, 1996). As the window size increases, more of the surface morphology within the reach contributes to the roughness metric being calculated. Thus, the roughness metric magnitude will typically increase with window size. This method has previously been implemented in topographic surface roughness calculations (Barabási & Stanley, 1995; Butler et al., 2001; Nield et al., 2013; Shepard et al., 2001; Smith, 2014), and is commonly implemented for evaluating semivariograms.
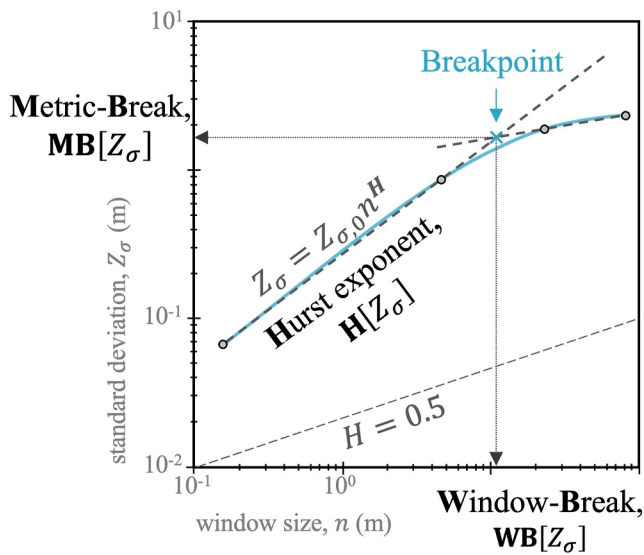
Figure 3. Graphical example representation of multi-scale metrics extraction (Metric-Break, Window-Break, and Hurst Component) based on break in slope of roughness metrics (here Z_σ) calculated over varying window sizes (n). The fitted dashed lines indicate the two fitted relationships to the roughness metric data. A Hurst component (H) of 0.5 is indicated. Adapted from Barabási and Stanley (1995) (Figure 2.3).

Breakpoints were extracted by detecting abrupt changes in the plotted slope of the logarithmic data series. A linear change detection method (`ischange` function, MATLAB) was applied to the logged data, which finds abrupt changes in the slope and intercept of the data using an iterative cost function (Killick et al., 2012). The maximum number of changes to detect was set to two. Once the points were identified, power trendlines were fitted between (a) the start of the datapoint, that is, the smallest window size, and the first abrupt change; and (b) the second abrupt change and the final datapoint. The intersection of these two fitted lines is taken as the breakpoint. This method can be robustly applied to all data sets. (Figure S1 in Supporting Information S1) provides detailed and zoomed-in clarifications of Z_σ and Ru_σ breakpoints for the BirkBeck site. Identifying the breakpoint enables the extraction of the associated metrics (a) "metric-break" MB - the roughness metric value associated with the breakpoint, and (b) "window-break" WB - the window size associated with the breakpoint. In an analysis of high-resolution data from gravel surfaces, these breakpoint scales have been suggested to distinguish between grain and form roughness (Butler et al., 2001).

Figure 3a presents an example of a multi-scale elevation standard deviation plot, whereby $MB[Z_\sigma]$ denotes the roughness metric magnitude at the breakpoint (Metric-Break), and $WB[Z_\sigma]$ denotes the corresponding window size (Window-Break) based on the moving window method. The bracketed nomenclature is modified based on the metric being represented. The power law relationship between the metric and window size at smaller length scales follows the form $Z_\sigma = Z_{\sigma,0} n^H$, whereby $Z_{\sigma,0}$ is the value at unit length scale, and H is the corresponding Hurst scaling exponent. As an example, the Hurst component is denoted in Figure 3 as $H[Z_\sigma]$. The Hurst exponents describe the self-affinity of a surface. When $H = 1$, the horizontal (window size) and vertical (roughness) metrics are self-similar and scale at the same rate, while $H < 1$ indicates that the roughness metric increases at a fixed but slower rate than the horizontal scale (Shepard et al., 2001). A random surface produced by Brownian motion would express $H = 0.5$ (Shepard et al., 2001).

An alternative method of multi-scale analysis using high-pass and band-pass filters was also applied to the entire surface. Surfaces were filtered with increasing wavelengths, and then metrics were calculated for each entire filtered surface (Buechel et al., 2022). Filter wavelengths ranged from 0.2 m (4 cells) up to the channel width ($w \cdot \Delta xy$ cells), in 200 logarithmic spaced steps. The high-pass filter retains all topographic wavelengths above the filter length, whereas the band-pass filter retains only wavelengths between the two filter lengths. For consistency between the two approaches, the midpoint of each filter step is plotted in outputs. Metrics calculated from band-pass filtering rather than moving window analysis are denoted by '$_{bp}$' subscript, and high-pass filtering by '$_{hp}$' subscript, for example, $MB[Z_{\sigma,hp}]$. As per the moving window analysis, we plotted the metric value against filter resolution and identified the break in slope to provide the corresponding breakpoint-based metrics (see Table 2). Here, the curve often does not saturate. Thus, the metric-break and window-break value is often the peak value. Surface roughness can also be quantified via Fourier transform methods (Stewart et al., 2019). However, this method cannot be conducted if there are any breaks in the data and so cannot be applied to our DEMs, as shown in Figure 1.

2.4. Statistical Analysis Methods

Co-variance between roughness metrics was quantified using the non-parametric Spearman's rank correlation coefficient (r_s) to identify the strength and direction of any monotonic, but not necessarily linear, relationships between metrics. Corresponding p-values < 0.01 were considered to have a statistically significant relationship, where the critical value of r_s is 0.534. We use this analysis to identify metrics that co-vary. This allows us to remove any highly correlated metrics to produce a subset of metrics that more uniquely capture the diversity of surface roughness in RBRs.
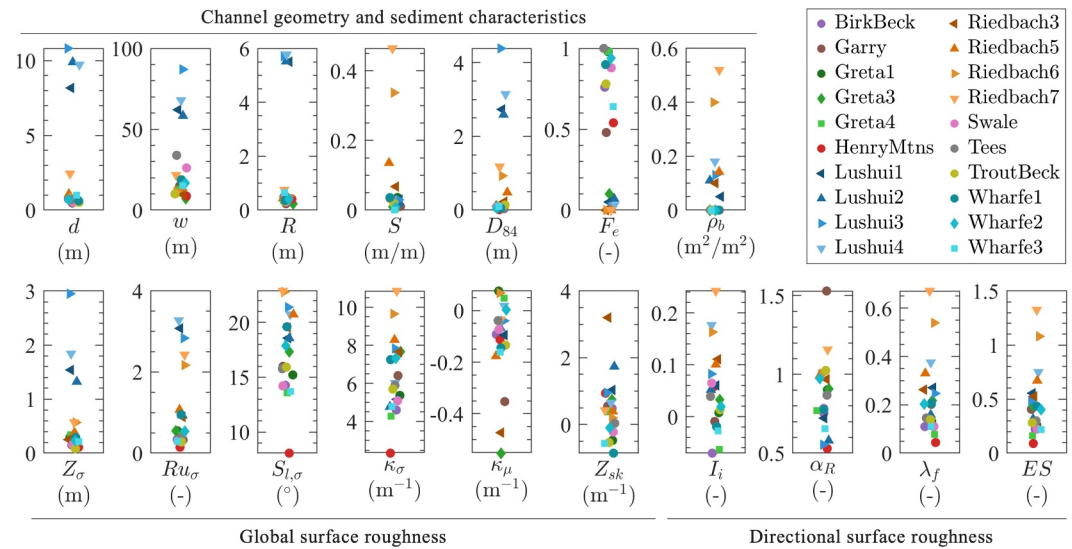
Figure 4. Distributions of channel geometric and sediment characteristics, global surface roughness metrics including directional-based metrics, as defined in Table 2. X-axis position is arbitrary to aid visualization between sites with similar metric values which are presented on Y-axis. Triangle symbols distinguish boulder-dominated channels.

Principal component analysis (PCA) was applied to the subset of surface roughness metrics. Z-score normalization was applied to the metrics prior to analysis. PCA implements linear orthogonal transformation to reveal the variance between metrics. The greatest variation in the data is represented by the first principal components (PC1), with subsequent components (i.e., PC2, PC3) explaining decreasing amounts of remaining variation. The contribution of each roughness metric to each principal component is referred to as the "loading." The principal component *scores* projects the data set into a coordinate space, aiding the identification of metrics that best differentiate between the different sites. A similar analysis was applied to sub-glacial topography by Woodard et al. (2021).

Hierarchical clustering (`clustergram` function, MATLAB) was applied to group sites according to similarity in roughness metric values, using a method based on the furthest Euclidean distances. This analysis was applied to the subset of roughness metrics selected in §3.3. Z-score normalization was again applied to the metrics prior to analysis. Optimal leaf ordering was applied to position adjacent sites or metrics with the greatest similarity, and dendogram grouping is presented with a threshold of 50% of maximum linkage. This analysis allowed the grouping of sites with comparable surface roughness values, hence enabling investigation of the contributing surface roughness metrics and associated bed features.

3. Results and Analysis

3.1. Channel Properties and Global Surface Roughness

The channel properties of the 20 sites encompass diversity in spatial scales and features. The basic channel geometric properties are presented in the upper panel of Figure 4 (see values in Table 1). The Lushui and Riedbach are both primarily boulder channels ("boulder-dominated") (F_e = 0.00 to 0.07), and the other sites are predominantly bedrock (F_e = 0.54 to 1.00), with the exception of Greta1 (F_e = 0.10). The channels range from wide-shallow rivers (e.g., Greta1, Figures 1 and a1) to the deeply incised gorges of the Lushui channel (Figures 1 and b1). The Lushui channels have higher channel depth (d), width (w), and hydraulic radius (R) than all other sites. Channel bed slopes (S) range from shallow gradients (<1%) to steep mountain reaches (up to 46.6% for site Riedbach7) (Figures 1 and d1). D_{84} values extend over an order of magnitude (although grain size data from the Lushui is based on boulders with a diameter greater than 1 m). Larger sediment grain sizes (D_{84}) are associated with the presence of boulders, with boulder density (ρ_b) of up to 52% at Riedbach7. Bedrock exposure (F_e) ranges from fully alluvial to fully bedrock, with sites such as HenryMtns featuring both exposed bedrock and alluvial areas with F_e = 0.54 (Figures 1 and c1). Smaller amounts of bedrock exposure are found in the Lushui, with no exposed bedrock in the Riedbach.

The lower panel in Figure 4 presents global roughness metrics (i.e., non multi-scale). The global elevation standard deviation (Z_σ) ranged from 0.08 m (TroutBeck) to 2.95 m (Lushui3), with the larger Z_σ values corresponding to sites with boulders (Figures 1 and b2). Boulder-bed sites also have higher values of Ru_σ and $S_{l,\sigma}$ although the range is less for these metrics, and there is overlap with non-boulder sites. Specifically, Ru_σ and $S_{l,\sigma}$ for Wharfe1 are larger than some boulder-bed sites, while HenryMtns $S_{l,\sigma}$ has the lowest magnitude. An overlapping transition between boulder and non-boulder channels is present for κ_σ, showing no clear distinction in surface curvature magnitude due to boulder presence, while HenryMtns has the lowest value. κ_μ assesses the dominant vertical direction of the curvature, with most sites expressing negative values (convex-out faces). The boulder-bed sites feature positive Z_{sk} values, caused by the vertical protrusions from the bed. The remaining channels span $Z_{sk} = -1$ to 1, revealing that some sites feature protrusions above the mean plane, including an isolated protrusion in HenryMtns, while others feature depressions (e.g., Wharfe1). Skewness provides important context as to whether positive directional (upstream facing) metrics correspond with obstruction to the flow.

The remaining plots in Figure 4 show the directional surface roughness metrics relative to the streamwise flow. I_i values are of greatest magnitude (positive and negative) for the boulder-bed sites. Positive values indicate a greater proportion of downstream-facing slopes. $\alpha_R < 1$ for most sites indicates that bed features align parallel to the flow direction, although a few sites exceed $\alpha_R = 1$, indicating more cross-stream facing cells than streamwise facing cells. The largest value of α_R is from Garry, where jointing perpendicular to the incoming flow is prevalent. The largest frontal solidity $\left(\lambda_f\right)$ values are associated with boulder-bed rivers due to blockage by the boulder faces. In contrast, lower values occur in the bedrock-exposed channels because fewer features protrude vertically from the bed. The data set reveals a continuous transition between sparse (isolated roughness, $\lambda_f \to 0$), hence smoother surfaces, and surfaces with denser arrays of obstacles.

3.2. Multi-Scale Surface Roughness

Multi-scale metrics reveal additional information, notably the length scales (window-break, WB[−]), the magnitude of roughness at this length scale (metric-break, MB[−]), and the rate at which metrics increase with increasing measurement length scale (Hurst exponent, $H[-]$). Figure 5 presents multi-scale plots for elevation-based metrics Z_σ, $Z_{\sigma,hp}$ and $Z_{\sigma,bp}$; and gradient-based metrics Ru_σ, $S_{l,\sigma}$ and κ_σ.

Z_σ roughness is positively correlated with the horizontal scale of analysis, with greater surface roughness magnitude when calculated over larger horizontal areas (window size, n). The convex shape of the curves in Figure 5a shows that most roughness is small scale, with ever-decreasing contribution from progressively larger scales as more of the overall channel morphology is included. Z_σ roughness increases with window sizes, as quantified by Hurst exponents in the region of H[Z_σ] = 0.50 shown by the dashed black line in Figure 5a. The greatest deviations from this trend include the Lushui sites (H[Z_σ] = 0.65 to 0.77), HenryMtns (H[Z_σ] = 0.61), and Greta1 and Greta4 (H[Z_σ] = 0.57) indicating a greater contribution to surface roughness at larger scales. Lower Hurst exponents reported for Greta3 (H[Z_σ] = 0.38) and TroutBeck (H[Z_σ] = 0.43) indicate that surface roughness is present at smaller scales but is not added to by larger scales. These results demonstrate that the Hurst exponent can potentially distinguish between channels with and without large protrusions or isolated boulders, although the presence of smaller-scale roughness is also influential. The Riedbach boulder channels were not distinguished by the Hurst exponent, likely due to the boulders and sediments fully covering the bed (not isolated elements). The higher H[Z_σ] value in HenryMtns is attributed to an isolated bedrock protrusion.

The window-break (and values below) represents the horizontal scales that dominate the main contributions to surface roughness, with values spanning an order of magnitude across the sites (Figure 5a). The lower gradient of the scale-metric plots at scales greater than the window-break indicates that there is less roughness contribution at larger scales. A larger window-break typically corresponds with a higher metric-break value, although there is notable scatter. The window-breaks associated with the boulder-bed rivers overlap the window-breaks of other sites, but their higher metric-break values reveal greater surface roughness. Across all non-boulder sites, the relationship between window-break and metric-break value follows a power relationship ($r^2 = 0.66$). For boulder sites, the relationship ($r^2 = 0.72$) has a significantly steeper trend, as denoted by the solid black lines in Figure 5a.

As an alternative to the moving window analysis, the frequency (wavelength) of surface roughness was evaluated using high-pass (Figure 5b) and band-pass filtering (Figure 5c). Z_σ roughness increases with filter resolution, showing that roughness magnitude is greater when longer frequency features are included. Results from high-pass
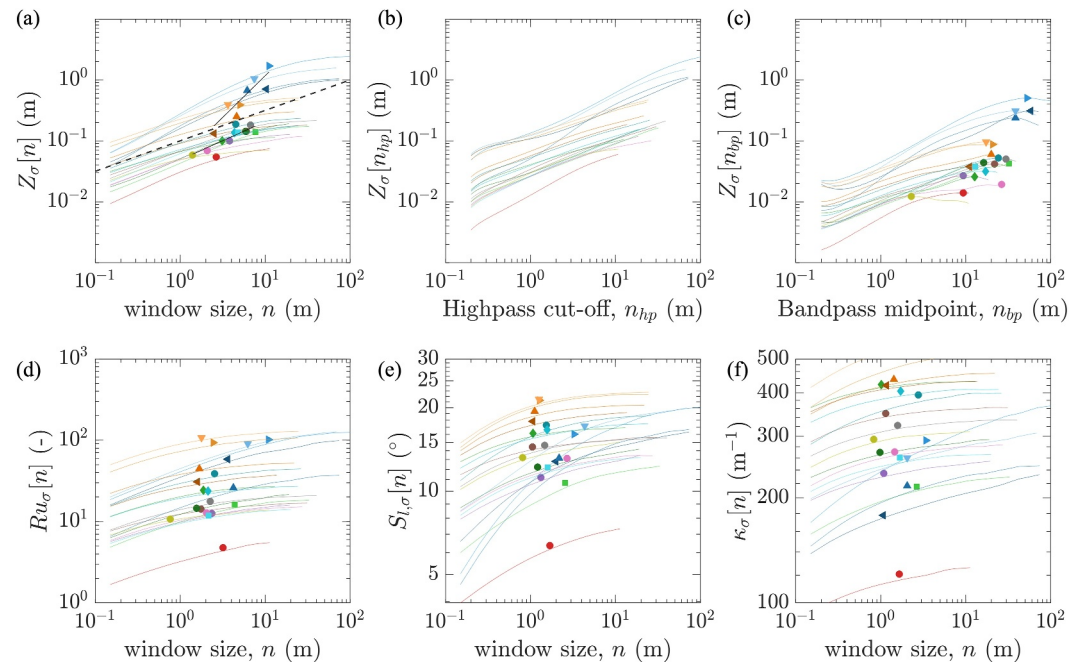
Figure 5. Multi-scale roughness metrics. See Figure 4 for legend or site symbols in Table 1 Colored lines in each plot (a–f) indicate each site, presenting the calculated metric value for at each window size, which are joined with straight lines. Markers show the location of the break in slope. In (a) the dashed line show a Hurst value of 0.5, and two power trendlines (solid black lines) are fitted for the boulder ($Z_\sigma[n] = 0.05n^{1.37}$; $r^2 = 0.72$) and non-boulder sites ($Z_\sigma[n] = 0.05n^{0.63}$; $r^2 = 0.66$), the 95% confidence bounds of the slope exponent of equations are [0.975, 1.763] and [0.472, 0.781].

results do not feature distinct breakpoints or dominant peaks, while small undulations in the overall trend are present, so differences between sites cannot be distinguished. Consequently, this metric is not used in further analysis. Band-pass filtering results in lower magnitude values of Z_σ due to the logarithmic filter spacing applied. Hence, a narrow filter range at shorter wavelengths retains a smaller range of roughness. The peaks in the signal, which correspond with the wavelength that most contributes to roughness, generally occur close to the maximum analysis length (the channel width), indicating that the largest roughness is associated with the channel form rather than smaller (grain or bed feature) scales. The metric-break and window-breaks associated with the band-pass peaks are used in subsequent analysis.

Multi-scale analysis of gradient- and curvature-dependent metrics (Figures 5d–5f) feature distinct breakpoints. Across the sites, most metric-breaks occur at similar window-breaks of around $n = 1$–4 m, suggesting that (a) these metrics may not be strongly dependent on the horizontal scale, or (b) these metrics are dominated by bed features and scales smaller than those defining Z_σ. Rugosity results (Figure 5d) provide some distinction between boulder and non-boulder channels, yet this is not as obvious as with $Z_\sigma[n]$, and there are also no clear trends shown by the corresponding breakpoints. Local slope and curvature results do not distinguish between channel types. Given that these metrics are calculated between neighboring cells, the extracted values represent roughness at the DEM resolution scale, and so do not capture the influence of longer scales (Shepard et al., 2001; Smith, 2014). This explains the lack of distinction between sites due to boulder presence, yet the output metrics H^{−}, WB[−], and MB[−] provide additional detail of the surface roughness and its properties, and represent different aspects of the roughness compared to the Z_σ metrics.

Normalization of metrics is not implemented at this stage, given the aim is to determine the absolute roughness of the river beds. The surface roughness relative to the channel properties is explored later in Section 3.6.

3.3. Correlation Between Surface Roughness Metrics: Feature Reduction

Correlation matrix analysis was conducted to test the co-variance between metrics. This enabled the identification of interchangeable metrics, and to establish a reduced set of independent metrics representing unique aspects of
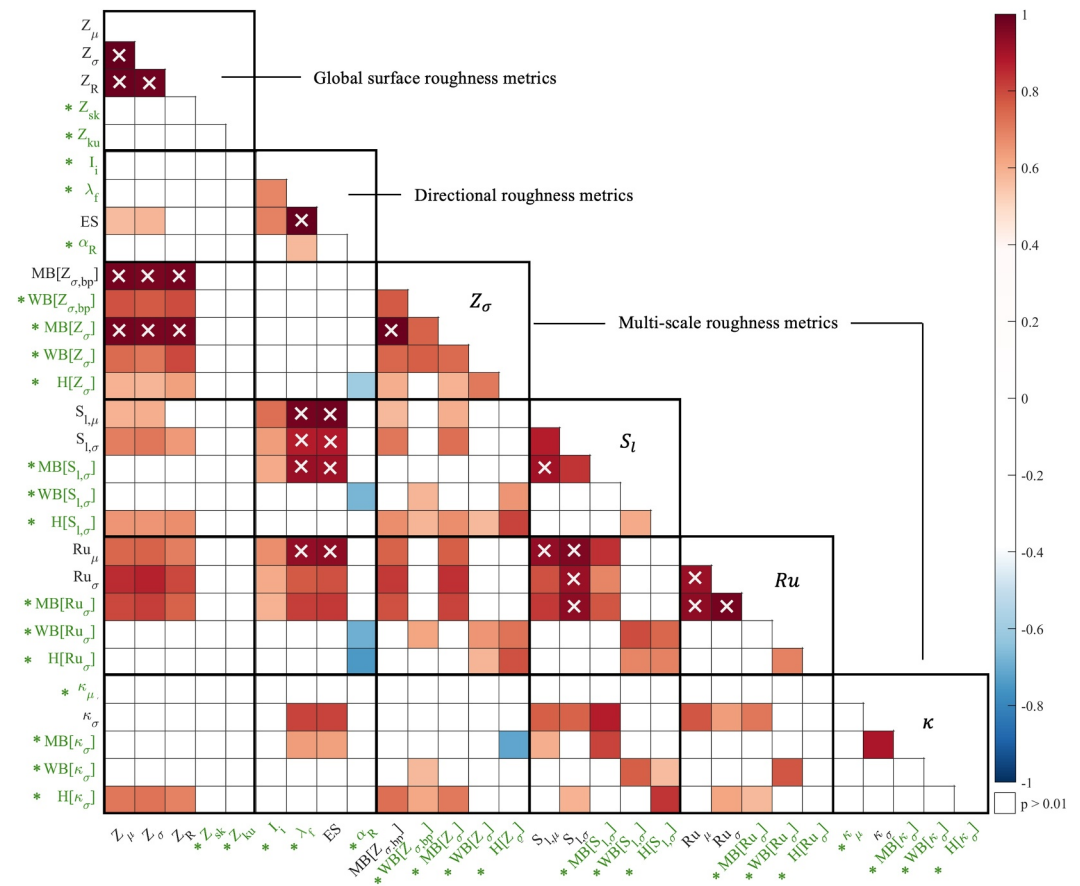
Figure 6. Correlation matrix of roughness metrics. Cell colors correspond to Spearman's Rank correlation coefficient, with white values below critical value ($r_s < 0.534$) with the relationships deemed not statistically significant ($p > 0.01$). Boxes with crosses have $r_s > 0.90$. Metric labels in green and with preceding "*" indicate those retained after feature reduction.

surface roughness. Spearman's rank analysis (Figure 6) revealed numerous statistically significant ($p < 0.01$) correlations between metrics, where the Spearman's rank correlation coefficient (r_s) critical value is 0.534. These relationships were evaluated to remove duplication by discarding some metrics from further analysis. Robust feature selection was performed by removing highly correlated metrics with a threshold of $|r_s| > 0.90$ (operated for each column in Figure 6). Ten metrics were deemed redundant, and the retained metrics are shown in green font in Figure 6. Strong correlations occur between global and multi-scale metrics obtained from the same base metric (e.g., Z_σ). The global metrics (mean and standard deviations) are predominantly redundant herein, and the multi-scale outputs are retained due to their additional spatial consideration.

Global surface elevation roughness metrics Z_μ, Z_R, Z_σ all have very strong correlations with one another ($r_s > 0.98$). Z_σ and MB[Z_σ] are also highly correlated but have different magnitudes. The global scale elevation metric is larger than the multi-scale metric (Figure 7a), which follows a power relationship of $Z_\sigma = 1.787 \cdot \text{WB}[Z_\sigma]$ ($r^2 = 0.98$). Although simpler global metrics provide a proportional representation of surface roughness, MB[Z_σ] is preferred due to its ability to represent surface elevation variability on multiple scales. MB[Z_σ] and WB[Z_σ] are moderately correlated, but closer inspection revealed two distinct trends for bedrock or boulder-bed sites (see Figure 5a), confirming their independence. MB[$Z_{\sigma,bp}$] is redundant due to the strong correlation with MB[Z_σ]. WB[$Z_{\sigma,bp}$], Z_{sk}, and Z_{ku} are not strongly correlated with any other metrics, making them unique metrics. The global metric κ_μ is unique, likely due to its inclusion of bidirectional (positive and negative) values that are not captured in multi-scale curvature metrics. λ_f strongly correlates with Ru-based metrics, with both representing the area of protrusions from the bed. However, λ_f provides additional directional information that could be lost if the metric was discarded at this stage. ES and λ_f are highly correlated (Figure 7b), such that these metrics can be used interchangeably with a relationship $ES = 0.5\lambda_f$ ($r^2 = 1$) given this is a
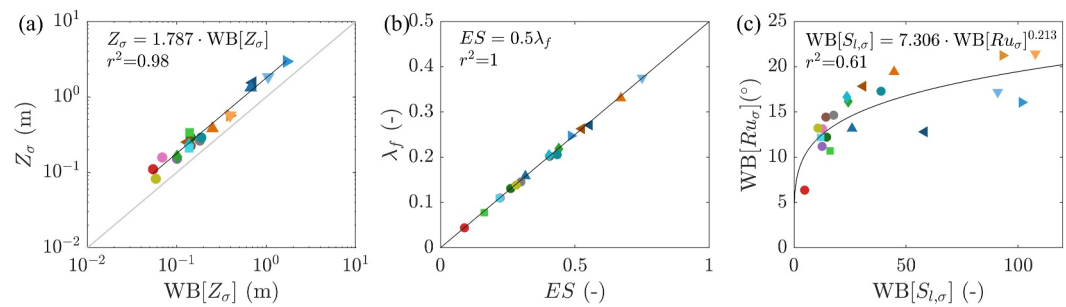
Figure 7. Relationships between surface roughness metrics. The gray line in (a) shows a 1:1 relationship. See Figure 4 for legend or site symbols in Table 1.

mathematical relationship (Napoli et al., 2008). The other directional-based metrics α_R and I_i are independent of other variables, these metrics are retained.

Metrics associated with rugosity (Ru_μ and Ru_σ) and local slope ($S_{l,M}$ and $S_{l,\sigma}$) are moderately correlated (Figure 7c). This is because they are both calculated from differences in elevation between adjacent cells, such that rugosity can be estimated from the local slope (cell gradient) (Powell et al., 2016). However, their correlations were not deemed sufficiently strong ($r_s < 0.90$) for either to be discarded. The corresponding Hurst exponents are retained for all multi-scale metrics as correlations are below the threshold ($r_s < 0.90$).

Subsequently, the following subset of metrics is found to provide an independent and unique quantification of the surface roughness of these RBRs. These are (a) Global metrics: $Z_{sk}, Z_{ku}, \kappa_\mu$; (b) Directional metrics: I_i, α_R, λ_f; and (c) Multi-scale MB[$-$], WB[$-$], and H[$-$] metrics for $Z_\sigma, S_{l,\sigma}, Ru_\sigma$ and κ_σ; along with WB[$Z_{\sigma,bp}$].

3.4. Principal Component Analysis

PCA confirms that the reduced set of roughness metrics all contribute to the first three principal components (Figures 8a–8c). The first three principal components explain 78.57% of the total variance, indicating that the variability in surface roughness is not fully represented by these components alone. This suggests that while these metrics capture the dominant roughness scales, additional metrics may be needed to fully define the roughness and that secondary scales may be influential.

The first principal component (PC1) represents the vertical and horizontal scales of the roughness, as shown by the positive loading associated with multiscale metrics in Figure 8a. This indicates a dependence on the multi-scale nature of surface roughness and represents the total roughness of the surface. The greatest contributors to PC2 are the directional metrics and the metric-break values of local slope, rugosity, and curvature. Thus, the second principal component (PC2) represents the slope-based and curvature metric-break measurements, including the surface features' directionality. The third principal component (PC3) represents the surface elevation PDF characteristics via the surface skewness and kurtosis, thus indicating the influence of the symmetry and spread of the surface elevations.

A spread in first and second principal component scores (PC1 and PC2 in Figure 8d) reveals variation in the channel morphology between the sites. Compared to the bedrock-dominated sites, the Lushui sites have higher PC1 but similar PC2 scores, indicating a greater magnitude of total surface roughness (PC1) but similar directional roughness (PC2). In contrast, the Riedbach sites have similar PC1 scores to the bedrock sites but higher PC2, indicating higher roughness at smaller scales as represented by the slope-based metrics. The Lushui sites feature boulders protruding from the bed, contributing to the large magnitude roughness shown by PC1. The higher PC2 values associated with the Riedbach site are associated with, higher density sediments and lower extent of exposed bedrock, resulting in closer packed roughness elements, hence smaller scale roughness.

3.5. Hierarchical Clustering

Hierarchical clustering reveals the similarity (or dissimilarity) between various entities. Nield et al. (2013) previously used dendrogram analysis to group surface roughness metrics and create links to observations of physical surface features and scales. The dendrograms in Figure 9 reveal the linkages between sites (left axis) or
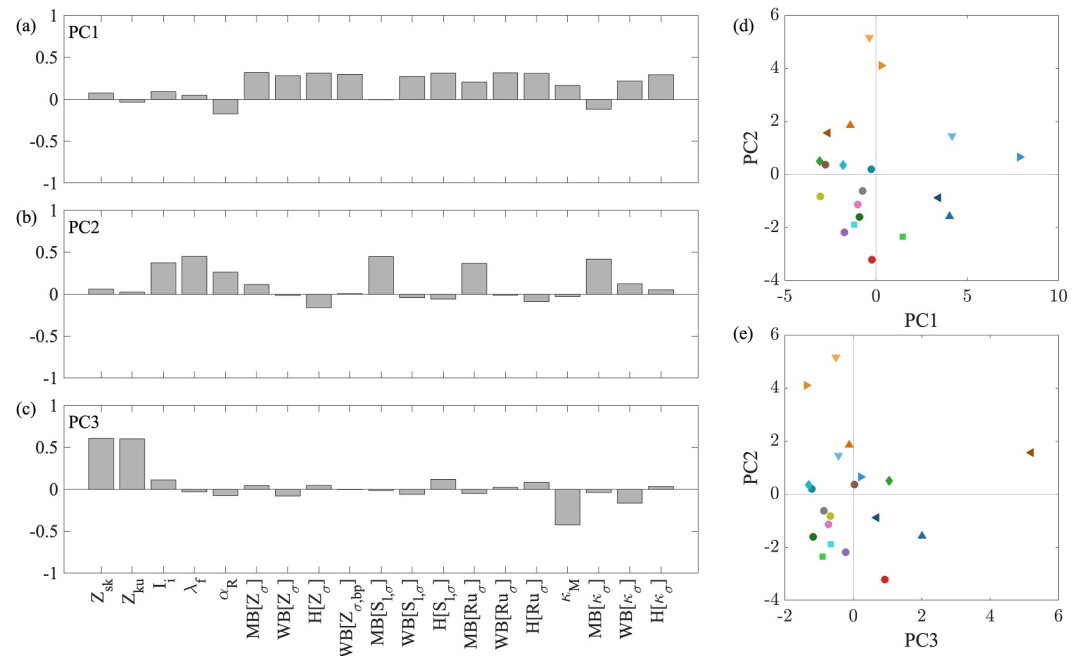
Figure 8. Metric coefficients (loadings) associated with the first three principal components (a) PC1 (43.04%), (b) PC2 (23.51%), (c) PC3 (12.02%); percentages indicate contribution of the total variance. (d) and (e) plots of PC1, PC2 and PC3. See Figure 4 for legend or site symbols in Table 1.

metrics (top axis). The level of similarity is indicated by the distance between dendrogram links, with smaller distances indicating greater similarity. For each site and metric, the corresponding clustergram heatmap indicates the Euclidean distance from the mean count (distance between site metric value and the data set mean), also called "relative expression" (Figure 9).

The horizontal-axis dendrogram in Figure 9 represents the similarity between roughness metrics, complementing the previous PCA analysis. The three metric groupings identified (M1, M2 and M3), for the most part, correspond to the first three principle components (PC1, PC2, and PC3). Hence, it is proposed that a metric from each of these categories is required to sufficiently distinguish surface roughness between differing rivers.

The vertical-axis dendrogram represents the similarity between sites, with five groupings presented (S1 to S5; Figure 9). Not all sites are included in a group if their similarity exceeds the linkage threshold (50%). Their groupings are evaluated herein with respect to the characteristics and channel topographic features.

Group S1 features primarily bedrock rivers devoid of boulders, except for the inclusion of Riedbach5, whose M2 values are not of great enough magnitude for it to be grouped into S2. The inclusion of Riedbach5 in S1 is likely due to its lower boulder density than other Riedbach sites and lower D_{84} values, resulting in its grouping with the sediment and bedrock-dominated sites. The scale of roughness in Riedbach5 has similarities with bedrock rivers, with close links to Greta3, which has a high sediment cover (limited exposed bedrock) and to the Garry, which features mixed sediment and distinct bedrock jointing. The remaining sites in this group are bedrock-dominated ($F_e = [0.64, 0.98]$).

Group S2 (Riedbach6 and Riedbach7) presents higher magnitude M2 metrics, which corresponds to the channels being fully alluvial ($F_e = 0.00$) with the small boulders that cover a notable portion of the bed ($\rho_b = 0.40$ and 0.52). Reidbach3 is ungrouped due to its large Z_{sk} and Z_{ku} values due to an isolated protruding element (boulder/bedrock outcrop) in the channel with elevation far exceeding the D_{84} (See Table S1 in Supporting Information S1).

The Lushui sites feature the highest magnitude horizontal and vertical roughness scales (M1 metrics) and are split into two groupings (S4 and S5). The large bed-roughness scales (shown by window-break) could be a product of the larger channel geometry relative to other sites. The larger Hurst exponents show the dominance of larger scale roughness over smaller scales. While Lushui has a large absolute roughness based on horizontal and vertical
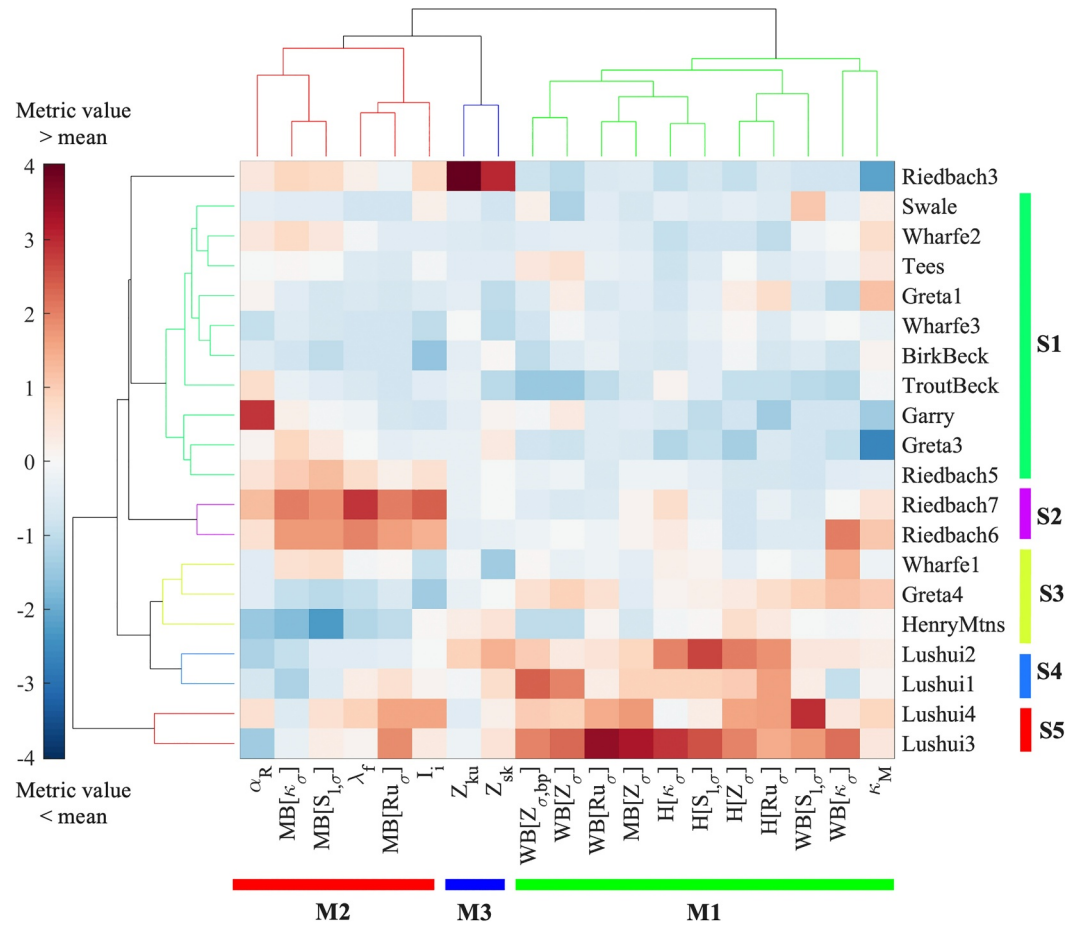
Figure 9. Hierarchical clustering between sites (S) and surface roughness metrics (M) and corresponding grouping. The colorbar represents the Euclidean distance from the mean count (distance between the site metric value and the data set mean). See Table 2 for metric abbreviations.

scales, this is not coupled with high magnitude directional and gradient-based metrics as are found in the Riedbach. This difference may occur because the boulders in the Lushui are larger, yet fewer in number, whereas the Riedbach has more boulders per unit area. S5 sites (Lushui3 and Lushui4) have higher boulder densities and sediment size ($\rho_b = 0.18$ and 0.13; $D_{84} = 3.143$ and 4.383) than S4 sites (Lushui2 and Lushui1) ($\rho_b = 0.11$ and 0.05; $D_{84} = 2.588$ and 2.730). The higher boulder densities in Lushui3 and Lushui4 are reflected in greater magnitude M2 metrics. It is interesting that the M2 magnitudes in S4 and S5 are not as high as those of the S2 Reidbach sites, despite the notably larger D_{84} in the Lushui sites. This emphasizes the importance of considering boulder density and spacing relative to the channel dimension and how this may influence flow resistance.

The distinctive characteristics of Group S3 (Wharfe1, Greta4, and HenryMtns) are less obvious as they have weaker deviations from the mean metric value (relative expression) relative to the other groupings. While they are primarily bedrock-dominated ($F_e = [0.54, 0.98]$), similar to S3, they generally feature negative M2 values combined with moderately positive M1 values, indicating lower slope- and area-based roughness (M2 metrics), yet positive (larger than the mean) spatial horizontal and vertical scales of the roughness (M1 metics).

Overall, these results demonstrate that it is not always possible to clearly distinguish channel roughness based on observation of channel type, nor are all boulder-dominated channels comparable. Instead, their topographic characteristics and surface roughness should be fully considered. Hence, in order to suitably describe and distinguish between RBRs, one must concurrently evaluate multiple topographic metrics encompassing (a) a vertical or horizontal scale-based roughness metric, (b) a slope or area-based metric, and (c) the elevation skewness or kurtosis.
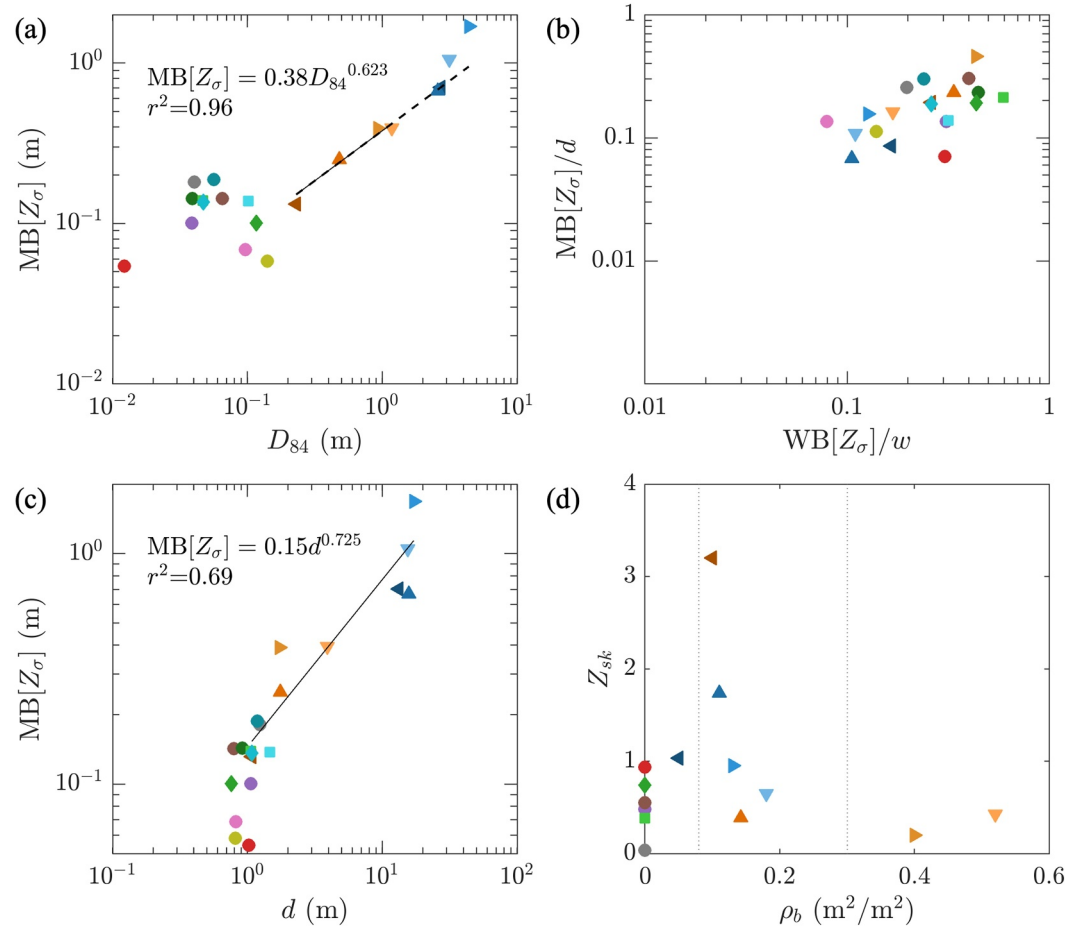
Figure 10. Comparison between surface roughness and channel properties. The following relationships are shown (a) sediment grain size (D_{84}) relative to Metric-Break of elevation standard deviation ($MB[Z_\sigma]$); (b) $MB[Z_\sigma]$ is normalized by channel depth (d), relative to the Window-Break of Metric-Break of elevation standard deviation ($WB[Z_\sigma]$) normalized by the channel width; (c) $MB[Z_\sigma]$) relative to d, with a trendline fitted to the boulder-bed sites; (d) boulder density $\left(\rho_b\right)$ relative to bed elevation skewness (Z_{sk}), with vertical lines showing ρ_b of 0.08 and 0.30.

3.6. Relationship Between Channel Properties and Surface Roughness

Finally, we evaluate relationships between surface roughness and channel properties. Our findings are compared to those identified by other authors. A particular focus is placed on the implications for flow resistance.

River bed roughness has previously been quantified using sediment grain size percentiles (D_{50} or D_{84}) or elevation standard deviation (Z_σ). In previous research on alluvial rivers, these metrics have strong linear correlations (Pearson et al., 2017). The reader is reminded here that Z_σ and $MB[Z_\sigma]$ can be used interchangeably when evaluating relationship correlation as they are directly proportional $\left(Z_\sigma = 1.79MB[Z_\sigma], r^2 = 0.98\right)$. Our data shows no coherent relationship between D_{84} and $MB[Z_\sigma]$ in the bedrock rivers (Figure 10a). It is expected that any correlations between D_{84} and $MB[Z_\sigma]$ would be more variable given that these sites feature differing amounts of sediment cover and include roughness associated with exposed bedrock. In the boulder-dominated Riedbach sites, a power relationship between D_{84} and $WB[Z_\sigma]$ is presented in Figure 10a (for comparison, Schneider et al. (2015) previously identified a power relationship between D_{50} and Z_σ). The Lushui sites plot along an extension of this trend (dashed trend line), albeit with increasing scatter. This may be attributed to the Lushui grain size data being for boulders greater than 1 m, or the lower channel slopes in the Lushui, with Schneider et al. (2015) reporting deviations for sites with gradients < 6%. Furthermore, it is noted that published relationships between D_{84} and Z_σ differ between different rivers (Pearson et al., 2017; Vázquez-Tarrío et al., 2017). X. Chen et al. (2020) showed that these relationships also vary between channel morphologies,

specifically with changes in bed gradient. However, we found no significant relationship between channel slope and MB[Z_σ] ($r_s = 0.382$, $p = 0.097$), with divergent trends for the Lushui and Riedbach sites.

Flow depth relative to bed roughness height (also called submergence ratio) is a fundamental control on flow resistance (Ferguson, 2007). Figure 10c presents a moderate correlation between roughness and depth in the boulder sites. In the bedrock sites, surface roughness can vary notably MB[Z_σ] = [0.05, 0.19] m in a maximum channel depth (d) between 0.76 and 1.24 m. Y. Chen et al. (2019) demonstrated that d/Z_σ is a primary control on flow resistance, and that horizontal length scales are a secondary control. Normalization of MB[Z_σ] by d (Figure 10b, y-axis) removes the distinction in absolute roughness values previously reported between boulder-bed and bedrock sites (Figure 5c). In all cases MB[Z_σ]/d < 1, showing that the bed is likely to be fully submerged at bankfull depth. The relative non-dimensional roughness, MB[Z_σ]/d, is higher in some of the bedrock rivers, and so flow resistance may also be higher in these channels. Inverting MB[Z_σ]/d gives the range 2.19 <d/MB[Z_σ] > 14.79, or 1.51 < Z_σ/d > 7.49.

Another way of normalizing the data is to divide the multi-scale window size (horizontal roughness scale) by channel width. Figure 10b reveals that although boulder-bed sites have high absolute values of WB[Z_σ] (Figure 5a), the magnitude of this window-break is lowered when channel width is considered. However, the normalized WB[Z_σ]/w values (Figure 7b, x-axis) span from 0.080 to 0.595. Consequently, surface roughness varies across channels and is not determined by the channel size alone.

Quantifying the density of boulders (ρ_b) and immobile bed elements is an alternative approach to evaluating surface roughness and flow resistance. Wiener and Pasternack (2022) reported that the majority of boulder-bed rivers have ρ_b between 0.08 and 0.30 (vertical dashed lines in Figure 10d), with most of our sites falling in this range. This range has been interpreted as evidence of river self-organization as it is associated with maximum flow resistance associated with turbulent wake production downstream of the boulders (Wiener & Pasternack, 2022). The argument of channel self-organization to maximize flow resistance has been widely proposed for step-pool sequences (Abrahams et al., 1995), yet it has also been shown that preferential spacing does not necessarily develop (Curran & Wilcock, 2005). This remains an open question in boulder-bed channels.

The use of ρ_b alone to evaluate flow resistance is challenging as it does not capture variation in vertical elevations, nor can it be applied to RBRs devoid of boulders. We find no relationship between ρ_b and MB[Z_σ]. Similar ρ_b values have notably different Z_σ magnitudes, indicating that boulder density alone does not capture the full topographic variability. Previous research has addressed this by coupling ρ_b with element protrusion to account for the vertical component required to predict roughness in boulder-bed channels (Lawrence, 2000; Yager et al., 2007). Furthermore, Nield et al. (2013), found that metrics based on surface height rather than obstacle spacing best predicted aeolian aerodynamic roughness length. The application of multiple surface roughness metrics presented in this paper offers promise to improve flow resistance prediction in boulder-bed channels, but would require testing against the established use of multiple element-based metrics.

A surface-based alternative to ρ_b is the frontal area metric, λ_f, which is applicable to all RBRs. It also includes information about the directionality of the roughness relative to the incoming flow. Another informative surface-based metric is skewness, which provides information on the distribution of roughness about the mean elevation and whether the surface is comprised of protruding elements (peaks) or hollows (pits). As boulder density increases, the skewness decreases toward zero for the channels with boulders, with the largest skew associated with fewer boulders (Figure 10d). The boulder-bed sites have positive skew, while negative skew occurs in bedrock sites where pits are caused by jointing in the bed (e.g., Wharfe3). Positive skew is more common in sites with more sediment cover. However, as Z_{sk} is a global metric, it also reflects any larger scale variations in the surface, including large depressions (e.g., negative skew in Greta1). MB[Z_σ] and Z_{sk} are independent of each other ($r_s = 0.257$, $p = 0.273$), suggesting skewness provides an additional topographic description.

While these metrics do not directly quantify the spacing of bed features, the relationship between λ_f and Z_{sk} can aid assessment of the shape and spatial nature of the surface roughness (Chung et al., 2021). Schematics in Figure 11 show idealized 1-D homogeneous bed topographies for different combinations of λ_f and Z_{sk} corresponding to our data. For the rough-bed channels, the largest λ_f values are associated with the boulder-bed channels, which also have positive skewness (Z_{sk}). As the schematics show, a high frontal area indicates densely packed or short wavelength roughness, corresponding with numerous tall protrusions per bed area. Within the boulder channels, Z_{sk} decreases as λ_f increases, following a trend that is not too dissimilar to the plot in
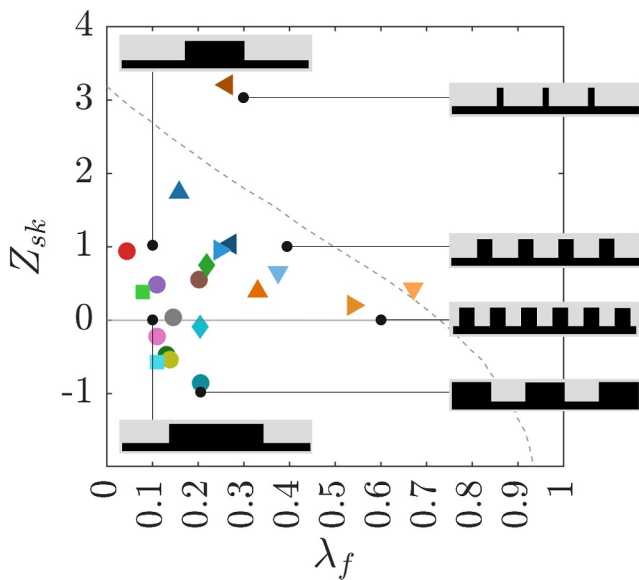
Figure 11. Relationship between site surface elevation skewness (Z_{sk}) and frontal solidity (λ_f), colored markers indicate measured sites. See Figure 4 for legend or site symbols in Table 1. The schematics surrounding the plot, and markers, show idealized homogeneous bed topographies (black areas) for different combinations of λ_f and Z_{sk}, resulting in differing block spacing and widths. This is inspired by Chung et al. (2021), and the dashed line shows the relationship of a cubic shaped and equally spaced obstacles.

Chung et al. (2021) for cubic features (gray dashed line), whereby the frontal area equals the plan area (i.e., cubes on a surface). In contrast, the bedrock channels feature shorter bed features relative to their planform area or small pits.

4. Discussion

4.1. Describing Rough-Bed River Topography

A range of surface roughness metrics were calculated and presented, including elevation, hybrid metrics based on elevation and spacing, and multi-scale metrics. It was found that many of these were interchangeable (e.g., $\lambda_f \propto ES$; MB$[Z_\sigma] \propto Z_\sigma$). Correlation analysis revealed a sub-set of metrics that were independent (no significant relationship) and potentially represented differing bed characteristics. We identified that the description and quantification of rough-bed surfaces require the assessment of global, directional, and multi-scale metrics.

Our PCA analysis found that a comprehensive description river bed topographic variability requires the concurrent use of multiple roughness metrics. The first three groups of the PCA analysis covered the first four moments of the distribution of elevations (Z_μ, Z_σ, Z_{sk}, Z_{ku}), and accounted for how they vary with window size. Consequently, a full and distinctive description of surface topography is likely to require multiple metrics. Our PCA findings are similar to those of Woodard et al. (2021), who found that the topography of glacial forelands was best described first by a principal component that described the entire DEM (roughness, slope, and curvature), and then by a second component comprised of directional metrics that quantified the asymmetry of the DEM. In contrast, Grohmann et al. (2010) found that metrics that best identified topographic features at a landscape scale included standard deviation of slope and curvature rather than the standard deviation of elevations, although their focus was a single DEM rather than a comparison between DEMs. Coleman et al. (2011) suggest that skewness (Z_{sk}) and kurtosis (Z_{ku}) can be used to identify between different alluvial bed types, again suggesting the importance of higher order moments of the distribution of elevations. Our finding that a complete set of surface roughness metrics should include surface skewness aligns with previous predictions of effective sandgrain roughness from multiple topographic metrics (Chung et al., 2021).

Variation between different channel types has been commonly observed; for example, X. Chen et al. (2020) identified different topographic relationships between different alluvial channels, including plane beds, step-pools and gravel dunes. The clustergram analysis used the metrics to group the beds into those with similar topographies. However, the identified groupings indicate that channels that might visually seem similar (e.g., the boulder-bed channels Lushui and Riedbach, and different reaches of bedrock channels with the same lithology, e.g., River Greta) can exhibit different topographic structures and fall into different groups. Consequently, assumptions about processes such as flow resistance should not be made based on channel type alone.

4.2. Implications for Flow Resistance

The flow velocity distributions and scales in the turbulent boundary layer are driven by surface roughness, in turn informing flow resistance. Velocity profile predictions include a roughness height to account for the influence of surface roughness, such as application in the power-law approach in gravel-bed rivers (Powell, 2014). This roughness height can be based on the D_{84} or more recently Z_σ (X. Chen et al., 2020). Yet, these surface elevation metrics alone do not fully represent the surface roughness and the influence on predicting velocities and flow resistance (Ferguson et al., 2024).

Despite its prevalence in predicting flow resistance in alluvial channels, our findings show unsurprisingly that D_{84} is a poor metric of channel roughness in bedrock channels. Even in the boulder-dominated channels, there is scatter in the relationship between D_{84} and MB$[Z_\sigma]$, in agreement with previous work such as Pearson et al. (2017). Z_σ is starting to be more widely used to predict velocity profiles and flow resistance (X. Chen

et al., 2020), with the increasing availability of topographic data from survey techniques such as TLS and SfM photogrammetry making that approach more feasible.

However, the use of Z_σ has still not been fully tested in fluvial settings, and X. Chen et al. (2020) show considerable scatter in their flow resistance predictions using Z_σ. This scatter is consistent with our finding that Z_σ does not account for all of the variations in topography between the different channels. Other work has looked at the impact of specific alternative metrics; for example, Flack et al. (2020) identified the importance of skewness in controlling flow resistance over rough surfaces. However, Busse and Jelly (2023) found that if high skewness is a product of an isolated element with extreme elevation deviation (as noted in the Riedbach3 site), the effect on the flow can be minimal, and so skew in isolation is unlikely to be sufficient.

This suggests that fully describing the impact of topography on flow resistance requires additional metrics to account for other components of the bed structure. Previous research has coupled element-based metrics (boulder density and protrusion) to predict flow resistance (Yager et al., 2007), or coupled surface roughness metrics (Z_{sk}, ES or λ_f) to predict effective sandgrain roughness (Chung et al., 2021; Forooghi et al., 2017). Hence, there is promise in the use of multiple surface roughness metrics to improve velocity profile and flow resistance predictions in RBRs instead of the use of Z_σ alone. In our data, Z_σ does not correlate with Z_{sk}, nor λ_f, so incorporating them into flow resistance predictions may provide additional predictive power (Deal, 2022). However, Flack et al. (2020) found that universal resistance predictions are more challenging for surfaces with a low effective slope (ES) due to low form drag contributions. Low effective slopes are reported in some of the bedrock-dominated sites presented in this paper, so the prediction of flow resistance in RBRs may not follow a universal predictive formula.

Our results also show that the roughness of the channel beds depends on the scale of analysis, consistent with previous work (Bertin et al., 2017; Hodge & Hoey, 2016a). Aberle et al. (2022) demonstrate the importance of directional roughness, whereby the same channel can produce differing flow resistance values if the relative flow direction is reversed. Flow resistance was larger in conditions when I_i was negative, and smaller when I_i was positive. However, flow resistance was also notably influenced by large-scale variation in cross-sectional area (channel narrowing and widening), emphasizing the need for further analysis of channel wall roughness variation. Hence, it is not clear what scale of roughness is most relevant for predicting flow resistance. Further research into the mechanisms by which topography causes flow resistance would provide insights into which metrics are most relevant and at which scales.

4.3. Implications for Sediment Transport and Sediment Cover

Understanding the impact of channel topography on flow is also important for evaluating sediment transport processes. In bedrock channels, variations in surface roughness between bedrock and alluvial areas of the bed will affect how flow resistance, shear stress and thus transport capacity change as sediment cover develops (Inoue et al., 2014; Johnson, 2014). The bedrock topography will also determine how easily sediment can collect on a bedrock surface (Hodge & Hoey, 2016b). Again, it is likely to be instructive to move beyond the use of just Z_σ. For example, bedrock surfaces exhibit both positive and negative values of Z_{sk}. Negative values indicate topographic hollows in which sediment is more protected from entrainment, although the volume of sediment that can be stored will depend on their spatial extent. Buechel et al. (2022) and Goode and Wohl (2010a) both found that grain entrainment depended on the directional structure of the channel bed, with Buechel et al. (2022) also identifying that entrainment is likely to be most affected by roughness at spatial scales comparable to the grain size. The variation in Hurst values between the bedrock surfaces means that even if surfaces exhibit similar properties at one scale, they may have different properties at the grain scale.

In boulder channels, topography will also influence the flow and thus sediment transport, but potentially at different scales compared to bedrock channels. In boulder channels, the dominant effect is likely to be the interactions between flow and boulders, reducing the shear stress available for sediment transport (Yager et al., 2007) and enabling locations of sediment deposition (Papanicolaou et al., 2018). The differing metrics may offer insight into channel formation processes, possibly reflecting differences in sediment sources and boulder mobility (Carr et al., 2023; Nitsche et al., 2012).

Ultimately, the bed surface roughness modulates the distribution of the velocity flow field above the bed, including the near-bed boundary layer properties. In turn, this influences the bed shear stress and sediment

transport. Depending on the scale of roughness, the bed and any sediments could be sheltered by larger roughness features, for example, regions downstream of large boulders.

4.4. Future Work and Considerations

Despite the increasing availability of high-resolution survey techniques, high-resolution topographic data of RBRs are still not widely available. In this work, we have collated a range of representative examples but acknowledge that certain channel types (e.g., highly sculpted bedrock (Wohl, 1998); or riffle-pool sequences) are missing from the analysis. Furthermore, our channels are relatively narrow (max width of 87.05 m), and so we do not know how this analysis would apply to larger channels (hundreds-of-meters, to kilometers), for example, the bedrock-alluvial Mekong River (Meshkova & Carling, 2012). Future research would benefit from a wider data set, the collection of which may be enabled through new bathymetric LiDAR technologies on both UAV and aircraft (Tonina et al., 2019). These LiDAR integrate measurements from above and below water, minimizing holes in the data and enabling the use of additional analytical methods, such as Fourier transforms (Perron et al., 2008).

Our analysis and quantification of surface roughness has also been limited to the channel bed of straight channels. The comparative roughness of channel walls and beds in RBRs influences how flow resistance changes with water depth (Ferguson et al., 2019), and so quantifying the topography of channel walls is an important next step. Other work could also extend this analysis to longer channel segments in order to incorporate the effect of components such as channel sinuosity and longitudinal steps.

The most suitable roughness metric for any application will depend on the metric that most closely controls the process of interest. However, in many cases further research is required to identify what that metric is, for example, through using new 3D printing and milling techniques to replicate field topographies in a flume (Hodge & Hoey, 2016a). It may not always be possible to apply any resulting metric-based relationships as there will still be situations where high-resolution data are not available or feasible. However, this research could also guide the development of empirical relationships between flow, sediment transport, and properties of the topography that can be measured without high-resolution DEMs, such as improved element-based methods. Research into sediment transport should consider which metrics best represent the impact of topography on the force-balance of individual grains, both via grain geometry (e.g., protrusion, pivot angle) and local hydraulics.

5. Conclusions

The channel topography of RBRs is an important control on flow and sediment transport processes. The increasing availability of high-resolution survey data (e.g., via SfM photogrammetry, TLS, bathymetric lidar) means that in many cases direct measurement of topography and roughness is increasingly feasible. However, we still do not know which roughness metrics best describe the impact of topography on flow and sediment transport processes. Here, we start by identifying the minimum set of metrics required to identify topographic differences between a set of RBR DEMs, and hence which metrics might offer most potential for future analysis.

We find that a comprehensive description of RBR topography requires the concurrent use of multiple roughness metrics to capture the surface roughness variability associated with multiple independent roughness elements and scales. We suggest that a complete set should include: (a) a vertical or horizontal scale-based roughness metric, with a recommendation to use the metric-break of surface elevation standard deviation; (b) a slope- or area-based metric, such as local slope, curvature, or rugosity; and (c) surface elevation skewness or kurtosis. In many applications (e.g., flow resistance), it would be advantageous to implement slope- and area-based metrics that encompass a directional measure relative to incoming bulk flow (α_R, I_i, and λ_f).

Using this set of metrics and their relative magnitudes in unison, we were able to separate RBRs into groups. These groups and the metric magnitudes were linked to the channel bed features and topography. One notable finding is that sites with boulders did not always have similar values of roughness metrics, indicating that sites that might seem similar based on common morphological classifications are grouped differently based on roughness. Alternative element-based metrics like boulder density did not capture the full variation between sites and would need to be coupled with a second metric such as boulder protrusion, as previous researchers have shown. We demonstrate that the availability of high-resolution topography data sets provides the ability to characterize river bed surface roughness using a host of metrics. Further research is required to enable evaluation of flow resistance

and sediment processes by concurrently implementing multiple surface roughness metrics rather than via more established element-based metrics.

Data Availability Statement

The data used in this paper is available via doi:10.5281/zenodo.14605934 (Houseago et al., 2024).

References

Aberle, J., Branß, T., Eikenberg, R., Henry, P. Y., & Olsen, N. R. B. (2022). Directional dependency of flow resistance in an unlined rock blasted hydropower tunnel. *Journal of Hydraulic Research*, *60*(3), 504–513. https://doi.org/10.1080/00221686.2021.2001596

Aberle, J., & Nikora, V. (2006). Statistical properties of armored gravel bed surfaces. *Water Resources Research*, *42*(11), W11414. https://doi.org/10.1029/2005wr004674

Aberle, J., & Smart, G. M. (2003). The influence of roughness structure on flow resistance on steep slopes. *Journal of Hydraulic Research*, *41*(3), 259–269. https://doi.org/10.1080/00221680309499971

Abrahams, A. D., Li, G., & Atkinson, J. F. (1995). Step-pool streams: Adjustment to maximum flow resistance. *Water Resources Research*, *31*(10), 2593–2602. https://doi.org/10.1029/95wr01957

Barabási, A.-L., & Stanley, H. E. (1995). *Fractal concepts in surface growth*. Cambridge University Press.

Bertin, S., Groom, J., & Friedrich, H. (2017). Isolating roughness scales of gravel-bed patches. *Water Resources Research*, *53*(8), 6841–6856. https://doi.org/10.1002/2016wr020205

Brasington, J., Vericat, D., & Rychkov, I. (2012). Modeling river bed morphology, roughness, and surface sedimentology using high resolution terrestrial laser scanning. *Water Resources Research*, *48*(11), W11519. https://doi.org/10.1029/2012wr012223

Buechel, M. E., Hodge, R., & Kenmare, S. (2022). The influence of bedrock river morphology and alluvial cover on gravel entrainment: Part 1. Pivot angles and surface roughness. *Earth Surface Processes and Landforms*, *47*(14), 3361–3375. https://doi.org/10.1002/esp.5463

Busse, A., & Jelly, T. O. (2023). Effect of high skewness and kurtosis on turbulent channel flow over irregular rough walls. *Journal of Turbulence*, *24*(1–2), 57–81. https://doi.org/10.1080/14685248.2023.2173761

Butler, J. B., Lane, S. N., & Chandler, J. H. (2001). Characterization of the structure of river-bed gravels using two-dimensional fractal analysis. *Mathematical Geology*, *33*, 301–330. https://doi.org/10.1023/A:1007686206695

Carr, J. C., & DiBiase, R. A. (2024). *Bedrock River channels of the Taiwan Central Range*. Distributed by OpenTopography. https://doi.org/10.5069/G9154F8F

Carr, J. C., DiBiase, R. A., Yeh, E. C., Fisher, D. M., & Kirby, E. (2023). Rock properties and sediment caliber govern bedrock river morphology across the taiwan central range. *Science Advances*, *9*(46), eadg6794. https://doi.org/10.1126/sciadv.adg6794

Chen, X., Hassan, M. A., An, C., & Fu, X. (2020). Rough correlations: Meta-analysis of roughness measures in gravel bed rivers. *Water Resources Research*, *56*(8), e2020WR027079. https://doi.org/10.1029/2020wr027079

Chen, Y., DiBiase, R., McCarroll, N., & Liu, X. (2019). Quantifying flow resistance in mountain streams using computational fluid dynamics modeling over structure-from-motion photogrammetry-derived microtopography. *Earth Surface Processes and Landforms*, *44*(10), 1973–1987. https://doi.org/10.1002/esp.4624

Chung, D., Hutchins, N., Schultz, M. P., & Flack, K. A. (2021). Predicting the drag of rough surfaces. *Annual Review of Fluid Mechanics*, *53*(1), 439–471. https://doi.org/10.1146/annurev-fluid-062520-115127

Coleman, S. E., Nikora, V. I., & Aberle, J. (2011). Interpretation of alluvial beds through bed-elevation distribution moments. *Water Resources Research*, *47*(11), W11505. https://doi.org/10.1029/2011wr010672

Curran, J. C., & Wilcock, P. R. (2005). Characteristic dimensions of the step-pool bed configuration: An experimental study. *Water Resources Research*, *41*(2), W02030. https://doi.org/10.1029/2004wr003568

Deal, E. (2022). Flow resistance in very rough channels. *Water Resources Research*, *58*(10), e2021WR031790. https://doi.org/10.1029/2021wr031790

Ferguson, R. (2007). Flow resistance equations for gravel-and boulder-bed streams. *Water Resources Research*, *43*(5), W05427. https://doi.org/10.1029/2006wr005422

Ferguson, R. I. (2022). Reach-scale flow resistance. In J. J. F. Shroder (Ed.), Treatise on geomorphology (Vol 6, pp. 110–132). Elsevier, Academic Press.

Ferguson, R. I., Hardy, R. J., & Hodge, R. A. (2019). Flow resistance and hydraulic geometry in bedrock rivers with multiple roughness length scales. *Earth Surface Processes and Landforms*, *44*(12), 2437–2449. https://doi.org/10.1002/esp.4673

Ferguson, R. I., Hardy, R. J., Hodge, R. A., Houseago, R. C., Yager, E. M., & Yamasaki, T. N. (2024). Predicting flow resistance in rough-bed rivers from topographic roughness: Review and open questions. *Earth Surface Processes and Landforms*, *49*(15), 4888–4907. https://doi.org/10.1002/esp.6016

Finnegan, N. J., Sklar, L. S., & Fuller, T. K. (2007). Interplay of sediment supply, river incision, and channel morphology revealed by the transient evolution of an experimental bedrock channel. *Journal of Geophysical Research*, *112*(F3), F03S11. https://doi.org/10.1029/2006jf000569

Flack, K. A., Schultz, M. P., & Barros, J. M. (2020). Skin friction measurements of systematically-varied roughness: Probing the role of roughness amplitude and skewness. *Flow, Turbulence and Combustion*, *104*(2–3), 317–329. https://doi.org/10.1007/s10494-019-00077-1

Forooghi, P., Stroh, A., Magagnato, F., Jakirlić, S., & Frohnapfel, B. (2017). Toward a universal roughness correlation. *Journal of Fluids Engineering*, *139*(12), 121201. https://doi.org/10.1115/1.4037280

Gomez-Heras, M., Ortega-Becerril, J. A., Garrote, J., Fort, R., & Lopez-Gonzalez, L. (2019). Morphometric measurements of bedrock rivers at different spatial scales and applications to geomorphological heritage research. *Progress in Earth and Planetary Science*, *6*(1), 1–18. https://doi.org/10.1186/s40645-019-0275-0

Goode, J. R., & Wohl, E. (2010a). Coarse sediment transport in a bedrock channel with complex bed topography. *Water Resources Research*, *46*(11), W11532. https://doi.org/10.1029/2009wr008135

Goode, J. R., & Wohl, E. (2010b). Substrate controls on the longitudinal profile of bedrock channels: Implications for reach-scale roughness. *Journal of Geophysical Research*, *115*(F3), F03018. https://doi.org/10.1029/2008jf001188

Grohmann, C. H., Smith, M. J., & Riccomini, C. (2010). Multiscale analysis of topographic surface roughness in the Midland Valley, Scotland. *IEEE Transactions on Geoscience and Remote Sensing*, *49*(4), 1200–1213. https://doi.org/10.1109/tgrs.2010.2053546

Hardy, R. J., Best, J. L., Lane, S. N., & Carbonneau, P. E. (2009). Coherent flow structures in a depth-limited flow over a gravel surface: The role of near-bed turbulence and influence of Reynolds number. *Journal of Geophysical Research*, *114*(F1), F01003. https://doi.org/10.1029/2007jf000970

Heritage, G. L., & Milan, D. J. (2009). Terrestrial laser scanning of grain roughness in a gravel-bed river. *Geomorphology*, *113*(1–2), 4–11. https://doi.org/10.1016/j.geomorph.2009.03.021

Hobson, R. (1972). Surface roughness in topography: Quantitative approach. In *Spatial analysis in geomorphology* (pp. 221–246). Routledge.

Hodge, R., Brasington, J., & Richards, K. (2009). Analysing laser-scanned digital terrain models of gravel bed surfaces: Linking morphology to sediment transport processes and hydraulics. *Sedimentology*, *56*(7), 2024–2043. https://doi.org/10.1111/j.1365-3091.2009.01068.x

Hodge, R. A., & Hoey, T. B. (2016a). A froude-scaled model of a bedrock-alluvial channel reach: 1. Hydraulics. *Journal of Geophysical Research: Earth Surface*, *121*(9), 1578–1596. https://doi.org/10.1002/2015jf003706

Hodge, R. A., & Hoey, T. B. (2016b). A froude-scaled model of a bedrock-alluvial channel reach: 2. Sediment cover. *Journal of Geophysical Research: Earth Surface*, *121*(9), 1597–1618. https://doi.org/10.1002/2015jf003709

Houseago, R., Hodge, R., Asher, B., Hardy, R., Ferguson, R., et al. (2024). Quantifying bed surface roughness in bedrock and boulder-bed rivers: Dataset. https://doi.org/10.5281/zenodo.14605934

Inoue, T., Izumi, N., Shimizu, Y., & Parker, G. (2014). Interaction among alluvial cover, bed roughness, and incision rate in purely bedrock and alluvial-bedrock channel. *Journal of Geophysical Research: Earth Surface*, *119*(10), 2123–2146. https://doi.org/10.1002/2014jf003133

Jenness, J. S. (2004). Calculating landscape surface area from digital elevation models. *Wildlife Society Bulletin*, *32*(3), 829–839. https://doi.org/10.2193/0091-7648(2004)032[0829:clsafd]2.0.co;2

Johnson, J. P. L. (2014). A surface roughness model for predicting alluvial cover and bed load transport rate in bedrock channels. *Journal of Geophysical Research: Earth Surface*, *119*(10), 2147–2173. https://doi.org/10.1002/2013jf003000

Johnson, J. P., & Whipple, K. X. (2007). Feedbacks between erosion and sediment transport in experimental bedrock channels. *Earth Surface Processes and Landforms*, *32*(7), 1048–1062. https://doi.org/10.1002/esp.1471

Killick, R., Fearnhead, P., & Eckley, I. A. (2012). Optimal detection of changepoints with a linear computational cost. *Journal of the American Statistical Association*, *107*(500), 1590–1598. https://doi.org/10.1080/01621459.2012.737745

Lane, S. N. (2005). Roughness – Time for a re-evaluation? *Earth Surface Processes and Landforms*, *30*(2), 251–253. https://doi.org/10.1002/esp.1208

Lawrence, D. S. L. (2000). Hydraulic resistance in overland flow during partial and marginal surface inundation: Experimental observations and modeling. *Water Resources Research*, *36*(8), 2381–2393. https://doi.org/10.1029/2000wr900095

Liu, Y., Stoesser, T., Fang, H., Papanicolaou, A., & Tsakiris, A. G. (2017). Turbulent flow over an array of boulders placed on a rough, permeable bed. *Computers and Fluids*, *158*, 120–132. https://doi.org/10.1016/j.compfluid.2017.05.023

McCarroll, D., & Nesje, A. (1996). Rock surface roughness as an indicator of degree of rock surface weathering. *Earth Surface Processes and Landforms*, *21*(10), 963–977. https://doi.org/10.1002/(sici)1096-9837(199610)21:10<963::aid-esp643>3.0.co;2-j

Meshkova, L. V., & Carling, P. A. (2012). The geomorphological characteristics of the Mekong River in northern Cambodia: A mixed bedrock–alluvial multi-channel network. *Geomorphology*, *147*, 2–17. https://doi.org/10.1016/j.geomorph.2011.06.041

Monsalve, A., Yager, E. M., & Schmeeckle, M. W. (2017). Effects of bed forms and large protruding grains on near-bed flow hydraulics in low relative submergence conditions. *Journal of Geophysical Research: Earth Surface*, *122*(10), 1845–1866. https://doi.org/10.1002/2016jf004152

Napoli, E., Armenio, V., & De Marchis, M. (2008). The effect of the slope of irregularly distributed roughness elements on turbulent wall-bounded flows. *Journal of Fluid Mechanics*, *613*, 385–394. https://doi.org/10.1017/s0022112008003571

Nield, J. M., King, J., Wiggs, G. F. S., Leyland, J., Bryant, R. G., Chiverrell, R. C., et al. (2013). Estimating aerodynamic roughness over complex surface terrain. *Journal of Geophysical Research: Atmospheres*, *118*(23), 12948–12961. https://doi.org/10.1002/2013jd020632

Nitsche, M., Rickenmann, D., Kirchner, J. W., Turowski, J., & Badoux, A. (2012). Macroroughness and variations in reach-averaged flow resistance in steep mountain streams. *Water Resources Research*, *48*(12), W12518. https://doi.org/10.1029/2012wr012091

Olaya, V. (2009). Chapter 6 basic land-surface parameters. In T. Hengl & H. I. Reuter (Eds.), *Geomorphometry* (Vol. 33, pp. 141–169). Elsevier. https://doi.org/10.1016/s0166-2481(08)00006-8

Papanicolaou, A. N., Tsakiris, A. G., Wyssmann, M. A., & Kramer, C. M. (2018). Boulder array effects on bedload pulses and depositional patches. *Journal of Geophysical Research: Earth Surface*, *123*(11), 2925–2953. https://doi.org/10.1029/2018jf004753

Pearson, E., Smith, M. W., Klaar, M. J., & Brown, L. E. (2017). Can high resolution 3d topographic surveys provide reliable grain size estimates in gravel bed rivers? *Geomorphology*, *293*, 143–155. https://doi.org/10.1016/j.geomorph.2017.05.015

Perron, J. T., Kirchner, J. W., & Dietrich, W. E. (2008). Spectral signatures of characteristic spatial scales and nonfractal structure in landscapes. *Journal of Geophysical Research*, *113*(F4), F04003. https://doi.org/10.1029/2007jf000866

Powell, D. M. (2014). Flow resistance in gravel-bed rivers: Progress in research. *Earth-Science Reviews*, *136*, 301–338. https://doi.org/10.1016/j.earscirev.2014.06.001

Powell, D. M., Ockelford, A., Rice, S. P., Hillier, J. K., Nguyen, T., Reid, I., et al. (2016). Structural properties of mobile armors formed at different flow strengths in gravel-bed rivers. *Journal of Geophysical Research: Earth Surface*, *121*(8), 1494–1515. https://doi.org/10.1002/2015jf003794

Schneider, J. M., Rickenmann, D., Turowski, J. M., & Kirchner, J. W. (2015). Self-adjustment of stream bed roughness and flow velocity in a steep mountain channel. *Water Resources Research*, *51*(10), 7838–7859. https://doi.org/10.1002/2015wr016934

Schwanghart, W., & Scherler, D. (2014). TopoToolbox 2 – MATLAB-based software for topographic analysis and modeling in Earth surface sciences. *Earth Surface Dynamics*, *2*, 1–7. https://doi.org/10.5194/esurf-2-1-2014

Shepard, M. K., Campbell, B. A., Bulmer, M. H., Farr, T. G., Gaddis, L. R., & Plaut, J. J. (2001). The roughness of natural terrain: A planetary and remote sensing perspective. *Journal of Geophysical Research*, *106*(E12), 32777–32795. https://doi.org/10.1029/2000je001429

Simons, D. B., & Richardson, E. V. (1961). Forms of bed roughness in alluvial channels. *Journal of the Hydraulics Division*, *87*(3), 87–105. https://doi.org/10.1061/jyceaj.0000612

Smart, G., Aberle, J., Duncan, M., & Walsh, J. (2004). Measurement and analysis of alluvial bed roughness. *Journal of Hydraulic Research*, *42*(3), 227–237. https://doi.org/10.1080/00221686.2004.9728388

Smith, M. W. (2014). Roughness in the earth sciences. *Earth-Science Reviews*, *136*, 202–225. https://doi.org/10.1016/j.earscirev.2014.05.016

Stewart, M. T., Cameron, S. M., Nikora, V. I., Zampiron, A., & Marusic, I. (2019). Hydraulic resistance in open-channel flows over self-affine rough beds. *Journal of Hydraulic Research*, *57*(2), 183–196. https://doi.org/10.1080/00221686.2018.1473296

Tonina, D., McKean, J. A., Benjankar, R. M., Wright, C. W., Goode, J. R., Chen, Q., et al. (2019). Mapping river bathymetries: Evaluating topobathymetric lidar survey. *Earth Surface Processes and Landforms*, *44*(2), 507–520. https://doi.org/10.1002/esp.4513

Vázquez-Tarrío, D., Borgniet, L., Liébault, F., & Recking, A. (2017). Using uas optical imagery and sfm photogrammetry to characterize the surface grain size of gravel bars in a braided river (vénéon river, French alps). *Geomorphology*, *285*, 94–105. https://doi.org/10.1016/j.geomorph.2017.01.039

Wiener, J. S., & Pasternack, G. B. (2022). Scale dependent spatial structuring of mountain river large bed elements maximizes flow resistance. *Geomorphology*, *416*, 108431. https://doi.org/10.1016/j.geomorph.2022.108431

Williams, R., Reid, E., & Roberts, K. (2022). Topographic point cloud of a bedrock reach of the river garry, scotland. https://doi.org/10.5525/gla.researchdata.1339

Wohl, E. E. (1998). Bedrock channel morphology in relation to erosional processes. In K. Tinkler & E. Wohl (Eds.), *Rivers over rock: Fluvial processes in bedrock channels*. American Geophysical Union.

Woodard, J. B., Zoet, L. K., Iverson, N. R., & Helanow, C. (2021). Variations in hard-bedded topography beneath glaciers. *Journal of Geophysical Research: Earth Surface*, *126*(9), e2021JF006326. https://doi.org/10.1029/2021jf006326

Yager, E. M., Kirchner, J. W., & Dietrich, W. E. (2007). Calculating bed load transport in steep boulder bed channels. *Water Resources Research*, *43*(7), W07418. https://doi.org/10.1029/2006wr005432